Velocity model building by 3D frequency-domain full-waveform inversion of wide-aperture seismic data

Hafedh Ben Hadj Ali*, Stéphane Operto† and Jean Virieux‡

*Géosciences Azur, CNRS, IRD, UNSA, UPMC, Valbonne, France. E-mail: benhadj@geoazur.unice.fr.

†Géosciences Azur, CNRS, IRD, UNSA, UPMC, Villefranche-sur-mer, France. E-mail: operto@geoazur.obs-vlfr.fr.

‡2 Laboratoire de Géophysique Interne et Tectonophysique, UJF, CNRS, Grenoble, France. E-mail: Jean.Virieux@obs.ujf-grenoble.fr.

(December 6, 2007)

Running head: **3D full waveform tomography**

ABSTRACT

We assess 3D frequency-domain acoustic full-waveform inversion data as a tool to develop high-resolution velocity models from low-frequency global-offset data. The inverse problem is based on a classic gradient method. Inversion is applied to few discrete frequencies allowing management of a limited subset of the 3D data volume. The forward problem is solved with a finite-difference frequency-domain method based on a massively parallel direct solver allowing efficient multiple-shot simulations involving several thousands of sources. The inversion code is fully parallelized for distributed-memory platforms taking advantage of a domain decomposition of the modeled wavefields performed by the direct solver. After validation on simple synthetic tests, full-waveform inversion was applied to two targets

(channel and thrust system) of the 3D SEG/EAGE overthrust model corresponding to 3D domains of $7 \times 8.8 \times 3.3$ km^3 and $13.5 \times 13.5 \times 4.65$ km^3 respectively. The maximum inverted frequencies were 15 Hz and 5 Hz for these 2 applications respectively. A maximum of 20 dual core biprocessor nodes with 8 gigabytes of share memory per node was used for the second case study. The main structures were successfully imaged at a resolution scale consistent with the inverted frequencies. This study confirms the feasibility of 3D frequency-domain full-waveform inversion of global-offset data on large distributed-memory platforms to develop high-resolution velocity models. Further work is required to [i] perform more representative applications on larger computational platforms, [ii] assess the sensitivity of the 3D full-waveform inversion to the acquisition geometry and to the starting model and [iii] assess whether velocity models developed by full-waveform inversion can be used as improved background model for prestack depth migration.

INTRODUCTION

Three-dimensional quantitative seismic imaging in complex environments such those involving deepwater, thrust belts, subsalt and subbasalt structures is one of the main challenge of seismic exploration for hydrocarbon exploitation. In the depth domain, the imaging flowchart for multichannel seismic reflection data is subdivided into 2 main steps: estimation of a velocity macromodel and prestack depth migration (PSDM). The first task is critical since the velocity macromodel has a strong impact on the accuracy of the migrated images in terms of focusing and positioning in depth of the reflectors. The criteria that must verify the velocity macromodel to provide accurate migrated images are still unclear (see Operto et al. (2000, 2003)) for some illustrations of the sensitivity of 2D and 3D true-amplitude PSDM to the accuracy of the velocity macromodel). Estimation of a reliable velocity macromodel for PSDM from conventional multichannel seismic reflection data is a difficult task which is even more dramatic in complex environments because of the velocity-depth ambiguity at significant depths. The most commonly-used approaches to build velocity model for PSDM rely either on reflection traveltime tomography (e.g., Stork (1992)) and migration velocity analysis (e.g., Yilmaz and Chambers (1984); Chauris et al. (2002)). Both approaches make approximations for modeling wave propagation such that the high-frequency approximation or the one-way approximation of the wave equation. This incomplete modeling of wave propagation together with the limitations imposed by narrow-aperture acquisition geometries, can preclude imaging of steeply dipping reflectors. For example, it was recently illustrated that turning waves and multi-reflected arrivals can contribute to improve imaging of the flank of salt bodies (Zhang et al., 2006). As a result, many efforts has been dedicated these last years to the extension of one-way propagator to exploit these arrivals in PSDM (e.g., Zhang et al. (2007)).

In this paper, we investigate frequency-domain full-waveform inversion (FWI) of wide-aperture data as a tool to build 3D high-resolution velocity model in complex environments (Pratt, 2004). By wide-aperture acquisition survey, referred in the following as global-offset acquisition, we mean any acquisition system with sufficiently long offset coverage to allow recording of turning waves whose refraction depth cover the zone of interest. Wide-aperture arrivals are primarily sensitive to the large and intermediate wavelengths of the medium which are difficult to image from multichannel seismic reflection acquisition and limited-bandwidth sources. Moreover, multifold wide-aperture surveys lead to a redundant control of frequency and aperture angle on the wavenumber illumination in the model space. This redundancy can be decimated to design efficient numerical approaches for seismic imaging in the frequency domain (Pratt, 1999; Pratt and Williamson, 1990). Global-offset acquisition survey may be carried out at sea and on land with a newtwork of ocean bottom and land stations respectively (see Clarke et al. (2007) for a recent 3D wide-azimuth node survey).

FWI refers to imaging method based on the complete solution of the full (two-way) wave equation for the forward problem and on inverse problem theory for the imaging problem (Tarantola, 1987). A model is built by minimization of the misfit between the recorded data and that computed in a starting model. The underlying imaging principle shares some similarities with generalized diffraction tomography (Wu and T*ö*ksoz, 1987; Pratt et al., 1998): the misfit wavefield is processed as the wavefield scattered by the missing heterogeneities in the starting model. These heterogeneities are processed as a series of closely-spaced diffractors. In virtue of Huygens' principle, image of the perturbation model is built by summation of the elementary images of each diffractors. The main drawbacks of FWI methods are two folds: first, they are very computationally expensive due to the complete resolution of the wave equation for a large number of sources. Second, they lack

robustness due to the complexity of the global-offset wavefields and their sensitivity to noise and to the inaccuracies of the starting model. During last decade, it was shown in the 2D case that the frequency-domain formulation of FWI applied to global-offset acquisition was providing a promising framework to mitigate these 2 difficulties. Aim of this paper is to start investigating the extension to 3D of this approach.

The frequency-domain formulation of FWI was originally developed for 2D cross-hole acquisition surveys which involve wide-aperture propagations (Pratt, 1999; Pratt and Williamson, 1990). Only few discrete frequencies are required to develop a reliable image of the medium thanks to the wavenumber redundancy provided by multifold wide-aperture geometries. Some guidelines to define the optimal frequency interval for FWI are given in Sirgue and Pratt (2004). This frequency-domain decimation leads to very compact volume of data to be managed which may be critical for 3D applications. Second, the frequency-domain formulation of FWI provides the most natural framework to design a hierarchical multiresolution imaging strategy which helps to manage the non linearity of the inverse problem by proceeding from the low frequencies to the higher ones (Pratt, 1999; Pratt et al., 1998; Pratt and Williamson, 1990). These two aspects (inversion of a limited subset of frequencies and successive inversion of increasing frequencies) allow to mitigate the two abovementioned drawbacks of FWI. Application of FWI to 2D real data case studies has been limited to frequencies smaller than 20 Hz (Ravaut et al., 2004; Operto et al., 2006; Shipp and Singh, 2002; Hicks and Pratt, 2001). In 3D, the computational cost of the forward problem suggests that it is difficult to handle frequencies greater than 10 hz for representative problems (Operto et al., 2007). At this resolution scale, the resulting velocity models can be conceived as improved velocity macromodel for PSDM. However, the relevance of FWI velocity models as reference model for PSDM still requires further demonstration. An illustration with a

real data case studies is provided in Operto et al. (2004, 2005) in the frame of the imaging of a thrust belt in the southern Apennines by combined first-arrival traveltime tomography, FWI and true-amplitude ray-based PSDM.

Full wave propagation modeling is a critical issue in FWI methods since it is the most computationally expensive task in the processing flow. In the frequency domain, the forward problem reduces to the resolution of a large sparse system of linear equations for each frequency to be considered. In the 2D case, the few frequencies involved in the inversion can be efficiently modeled for multiple shots using a direct solver (Marfurt, 1984). Since the original work of Pratt and Williamson (1990), optimal finite-difference stencils were designed for the frequency-domain method based on direct solvers (Jo et al., 1996; Hustedt et al., 2004; Stekl and Pratt, 1998). The extension to 3D of this modeling approach was addressed in Operto et al. (2007) who showed that problems of representative size (e.g., the 3D SEG/EAGE overthrust model) can be addressed at low frequencies (< 10 Hz) on currently-available distributed-memory platforms. However, it remains unclear which approach (time versus frequency domain, frequency-domain approach based on direct or iterative solvers) is the most efficient one for 3D full-waveform inversion (Plessix, 2007). This may depend on several parameters related to the experimental setup such that the dimensions of the model, the frequency bandwidth, the number of traces in the acquisition and the acquisition geometry. Three-dimensional frequency-domain modeling methods based on iterative solvers have been recently presented in Plessix (2007); Riyanti et al. (2007); Warner et al. (2007). These approaches are far less memory demanding than that based on direct solvers but their run times depend linearly on the number of sources which may be a significant drawback in the case of 3D surveys involving several thousands of shots or receivers.

Aim of this paper is to provide some preliminary insights on the feasibility and rele-

vance of 3D frequency- domain FWI for building high-resolution velocity models of isotropic acoustic media. Few applications of 3D frequency-domain FWI to synthetic models have been recently presented by Stekl et al. (2007); Sirgue et al. (2007); Ben-Hadj-Ali et al. (2007). Some critical issues related to 3D FWI will not be addressed in this paper and will be left for further investigations. These issues are the building of a reliable starting model for FWI which is conventionally carried out by first-arrival traveltime tomography when global offset acquisitions are considered (Brenders and Pratt, 2006a,b; Ravaut et al., 2004). We will assume in the following that a starting model describing the long wavelengths of the true medium is available. The second issue is the design of 3D global offset acquisition surveys suitable for 3D first-arrival traveltime tomography and FWI. Some footprints of the azimuth coverage on 3D FWI was recently illustrated by Sirgue et al. (2007) thanks to an application to the 3D SEG/EAGE overthrust model. Numerical examples presented in this paper are focused on surface global-offset surveys carried out with networks of source and receiver on the surface.

In the first part of the paper, we briefly review the theory of frequency-domain full-waveform modeling and inversion. In the second part, we discuss the parallel implementation of frequency-domain FWI for distributed-memory platforms. In the third part, we present several numerical examples of increasing complexities whose aim is to validate the algorithm, to illustrate the sensitivity of the imaging resolution to the acquisition geometry and to provide some insights on the computational complexity of the approach for representative case studies.

THEORY

Theory of frequency-domain full-waveform modeling and inversion will not be rehashed in this paper since it is now a well-established method for imaging 2D media. The extension to the 3D case closely follow the strategies that has been developed in 2D. Therefore, only a brief review of frequency-domain modeling and inversion will be given here. The reader is referred to Operto et al. (2007) for the method used in this paper for frequency-domain wave propagation modeling, Pratt et al. (1998) for theoretical aspects of frequency-domain FWI and Pratt (1999) for more practical aspects such that waveform inversion data preprocessing and source estimation.

3D acoustic finite-difference frequency-domain modeling

The 3D visco-acoustic wave equation in the frequency domain is given by

$$\begin{aligned} &\tfrac{\omega^2}{\kappa(x,y,z)} P\left(x,y,z,\omega\right) + \tfrac{\partial}{\partial x}\left(\tfrac{1}{\rho(x,y,z)}\tfrac{\partial P(x,y,z,\omega)}{\partial x}\right) \\ &+\tfrac{\partial}{\partial y}\left(\tfrac{1}{\rho(x,y,z)}\tfrac{\partial P(x,y,z,\omega)}{\partial y}\right) + \tfrac{\partial}{\partial z}\left(\tfrac{1}{\rho(x,y,z)}\tfrac{\partial P(x,y,z,\omega)}{\partial z}\right) \\ &= -S\left(x,y,z,\omega\right) \end{aligned} \tag{1}$$

where $\rho\left(x,y,z\right)$ is density, $\kappa\left(x,y,z\right)$ is the bulk modulus, ω is frequency, $P\left(x,y,z,\omega\right)$ is the pressure field and $S\left(x,y,z,\omega\right)$ is the source. Sponge-like PML (Perfectly Matched Layer) at edges of the necessary limited numerical model can be easily implemented in the frequency domain to absorb energy (Berenger, 1994; Operto et al., 2007).

Since the relationship between the pressure wavefield and the source is linear, the discrete acoustic wave equation (1) can be recast in a matrix form as

$$\mathbf{A}\ \mathbf{p} = \mathbf{s} \tag{2}$$

where the complex-value impedance matrix **A** depends on the frequency and the medium properties.

The system 1 can be discretized with the so-called parsimonious mixed-grid finite-difference method (Jo et al., 1996; Hustedt et al., 2004; Operto et al., 2007). The mixed-grid discretization which consists of the discretization of the differential operators on different rotated coordinate systems is complemented by a mass-term distribution (an anti-lumped mass) which allows to significantly improve the accuracy of the stencil (Marfurt, 1984). The combined use of the mixed coordinate systems and the mass distribution allows to design both accurate and spatially-compact stencil. A dispersion analysis demonstrates that only 4 grid points per wavelength are enough to obtain accurate simulations in homogeneous media. This discretization rule is optimal for FWI whose resolution limit is $\lambda/2$ where λ is the wavelength. Use of compact stencil is critical if a direct method is used to solve the system resulting from the discretization of the Helmholtz equation because compact stencils allow to limit the numerical bandwidth of the matrix and hence its fill-in during LU factorization. Use of direct solver is interesting in the case of multiple-shot simulations as those required by tomographic applications since the LU factorization is independent of the right-hand side terms in equation 2. To solve system 2, we use the massively parallel direct solver MUMPS which has been developed for distributed-memory platform (Amestoy et al., 2007). A detailed complexity analysis of this approach is provided in Operto et al. (2007).

Frequency-domain full-waveform inversion

The inverse problem is solved by a classic weighted least-squares gradient method (Tarantola, 1987). Newton and quasi-Newton (Gauss-Newton) methods were rejected because of

the computational cost of either the Hessian or the approximate Hessian (Pratt et al., 1998). The weighted least-squares cost function is given by

$$\mathcal{C}(\mathbf{m}) = \Delta\mathbf{d}^{\dagger}\mathbf{W}_d\Delta\mathbf{d} \tag{3}$$

where $\Delta\mathbf{d}$ is the misfit function (the difference between the observed data and the data computed with model $\mathbf{m}$), the superscript † indicates the adjoint (transpose conjugate) and $\mathbf{W}_d$ is a weighting operator applied to the data which scales the relative contribution of each component of the vector $\Delta\mathbf{d}$ in the inversion. Minimization of the cost function leads to the following solution for the model perturbation $\Delta\mathbf{m}$ after scaling and smoothing of the gradient (Pratt et al., 1998; Ravaut et al., 2004; Operto et al., 2006).

$$\Delta m_i = -\alpha \left(diag\mathbf{H}_a + \epsilon I\right)^{-1} \mathcal{G}_{\mathbf{m}} Re\left\{\mathbf{p}^t \left[\frac{\partial \mathbf{A}^t}{\partial m_i}\right] \mathbf{A}^{-1}\mathbf{W}_d\Delta\mathbf{d}^*.\right\} \tag{4}$$

where $diag\ \mathbf{H_a} = diagRe\{\ \mathbf{J}^t\ \mathbf{W}_d\ \mathbf{J}^*\}$ denotes the diagonal elements of the weighted approximate Hessian $\mathbf{H_a}$ and $\mathbf{J}$ denotes the sensitivity matrix.

One element of the sensitivity matrix is given by

$$\mathbf{J}_{k(m,n),i} = \mathbf{p}_m^t \left[\frac{\partial \mathbf{A}^t}{\partial m_i}\right] \mathbf{A}^{-1}\delta_n. \tag{5}$$

where $k(m,n)$ denotes a source-receiver couple of the acquisition system, m and n denotes respectively a shot and a receiver position. δ_n is an impulsional source located at the receiver position n.

The diagonal of the approximate Hessian provides a preconditioner of the gradient which properly scales the perturbation model (Shin et al., 2001). The damping parameter ϵ is used to avoid numerical instabilities (i.e. division by zero). The matrix $\mathcal{G}_{\mathbf{m}}$ is a smoothing regularization operator. It is implemented in the form of a 3D Gaussian spatial filter whose

correlation lengths are adapted to the inverted frequency component (Ravaut et al., 2004). An amplitude gain with offset can applied to each seismic trace within the operator $\mathbf{W}_d$

$$w_d(o_{sr}) = exp(gLog\,|o_{sr}|) \tag{6}$$

where the scalar g controls the amplitude of the gain with respect to the source-receiver offset o_{sr}. In our algorithm, the scaling of the gradient could be estimated once per frequency before the first iteration and kept constant over iterations or re-computed at each iteration. The term $\frac{\partial \mathbf{A}}{\partial m_i}$ is the radiation pattern of the diffraction by the model parameter m_i. In the case of the P-wave velocity, this radiation pattern is that of an explosion. In other words, this matrix reduces to one scalar. The source term can be estimated in the FWI algorithm by solving a linear inverse problem (Pratt, 1999). The inversion code can be applied to vertical geophone data or to hydrophone data generated by explosive sources. Indeed, vertical geophone data can be processed as pressure data thanks to the reciprocity principle (Operto et al., 2006). The inversion is applied in cascade to several groups of discrete frequencies. All the frequencies of one group are inverted simultaneously. The final model obtained close to inversion of one group of frequencies is used as a starting model for the next group of frequencies. For each frequency group, several iterations can be computed.

PARALLEL NUMERICAL IMPLEMENTATION

We use the massively parallel direct solver MUMPS (Amestoy et al., 2006, 2007) based on a multifrontal method (Duff and Reid, 1983) to solve the forward problem (system 2). Before LU decomposition, the matrix coefficients are ordered so that dependencies in the graph of the matrix are minimized. Using nested dissection ordering, the theoretical memory complexity of the factorization for a 3D FD problem is $O(n^4)$ and the number of floating-

point operations is $O(n^6)$ where n is the number of grid points along one dimension of the 3D square FD grid (Ashcraft and Liu, 1998). The source vectors for the resolution phase are provided in sparse format on the host processor. After resolution, the multiple solutions are distributed over processors following a domain decomposition driven by the distribution of the LU factors. This means that each processor stores a spatial sub-domain of all the solutions. We take advantage of this distributed in-core storage of the forward problem solutions to solve in parallel the inverse problem.

The central component of the FWI algorithm is the computation of the gradient of the cost function. This operator is basically computed by a weighted summation of the forward problem solutions (FPS), namely, the incident and the backpropagated residual wavefields computed in the starting model, equation 4. The weights in the summation account for the radiation pattern of the diffraction tomography reconstruction (the operator $\left[\frac{\partial \mathbf{A}^t}{\partial m_i}\right]$ in equation 5) and for the data residuals. This weighted summation is computed in parallel in a straightforward way by taking advantage of the distribution of the FPSs: each processor computes the subdomain of the gradient corresponding to the subdomain of the FPSs stored on this processor. At the end of the summation, the distributed gradient is gathered on the master processor with a collective communication. Note that, when only the P-wave velocity parameter is involved in the inversion, the matrix $\left[\frac{\partial \mathbf{A}^t}{\partial m_i}\right]$ reduces to a scalar located on the i^{th} diagonal. This implies that the gradient at position of m_i only depends on the values of the FPSs at this same position. In that case, the parallel computation of the gradient doesn't require any point-to-point communication leading to a parallelism efficiency close to 1 for the gradient computation. Note also that all the FPSs remain in core in the algorithm. No disk swapping is used in the current algorithm. If no enough memory is available to store in core all the FPSs in addition to the LU factors, the computation of the multi-RHS

resolution with MUMPS, of the gradient and of the Hessian is performed in a sequential loop over partitions of RHS terms. Each partition loads in core the maximum number of solutions fitting the available memory. The efficiency of the parallel inversion algorithm is mainly controlled by that of the LU factorization. We obtain a maximum speed-up of 13 with the MUMPS direct solver on our applications (Operto et al., 2007).

The parallel FWI algorithm is summarized in Figure 1.

SYNTHETIC EXAMPLES

In this section, we present several numerical examples of 3D FWI of increasing complexities to validate the algorithm and to give some insights on the computational cost of the approach on realistic cases. All applications presented hereafter were computed on a HP DL 145G2 Beowulf cluster of computer center SIGAMM host by Observatoire de la Cote d'Azur (France). This parallel distributed computer is a 48 dual node cluster machine with 2.4 GHz bi-processors with a 19.2 Gflops peak performance per node. This computer has a distributed memory architecture, where each node has 8 GBytes of RAM. The interconnection network between processors is Infiniband 4X. Data sharing among processors is performed using the message passing library MPIHP. For all the examples presented hereafter, the PML layers spread along 5 grid points on each side and each direction. These PML grid points are not taken into account in the description of the finite-difference grids.

3D full-waveform inversion in 2D configuration

In a first step, we validate the 3D FWI algorithm by comparing the results obtained using a 2D FWI code and the 3D one applied in a 2D configuration. Two-dimensional experiments

can be designed considering 2.5-D velocity models (laterally invariant in the y-direction) and an infinite line source in the y direction. The infinite line source in the y direction was implemented on a limited computational domain in the y direction using periodic boundary conditions on the two faces of the model corresponding to $y = 0$ and $y = y_{max}$.

The periodic boundary conditions that were implemented are

$$\left[\frac{\partial P}{\partial y}\right]_{y=-h/2, y_{max}+h/2} = 0 \tag{7}$$

They are applied on two virtual ghost faces located outside the computational domain at positions $y = -h/2$ and $y = y_{max} + h/2$ where h stands for the grid interval.

We applied 3D and 2D FWI to a dip section of the overthrust model (Aminzadeh et al., 1997) (Figure 2(a)), discretized on a 801×187 grid with a grid spacing $h = 25$ m. For the 3D application, the dip section of the overthrust model was duplicated 5 times in the y direction leading to a 3D $801 \times 5 \times 187$ finite-difference grid. A 2D wavefield computed in this 2.5D model with the above mentioned boundary conditions is shown in Figure 3.

The starting model for inversion is obtained by smoothing the true velocity model with a Gaussian function of horizontal and vertical correlation lengths of 500 meters (Figure 2(b)). To obtain stable inversion, the true velocity structure was set in the first 100 meters of the starting model. The 2D acquisition system consists of a line of 200 sources and receivers equally-spaced on the surface. The corresponding 2.5D acquisition system consists of duplicating 5 times the source and receiver lines in the y direction. We inverted sequentially 7 frequencies ranging from 5 to 20 Hz. For each frequency, we compute 10 iterations. The final velocity models inferred from 2D and 3D FWI are shown in Figure 4. Some vertical graphs extracted from these models are compared in Figures 5. They are very similar hence,

providing a first validation of the 3D FWI algorithm. The agreement between the final FWI models and the true model is also quite good. Some high-amplitude perturbations are still underestimated mainly due to an insufficient number of iterations (Figures 5). These results also give some insights on the high spatial resolution which can be achieved in the velocity models at relatively low frequencies (i.e., < 15 Hz) by FWI of global offset data thanks to the continuous sampling of the wavenumber spectrum up to a maximum wavenumber of $2/\lambda_{15Hz}\ m^{-1}$ (λ_{15Hz} denotes wavelengths corresponding to a frequency of 15 Hz).

Inclusion models

In this section, we present application of 3D FWI for simple velocity models composed of homogeneous background with one or two inclusions. The models are discretized on a small $31 \times 31 \times 31$ grid with 250 m cubic cells. The velocity in the background medium is 4000 m/s. The inverted frequencies are 1.75, 2.35, 3 and 3.75 Hz. Shots and receivers are uniformly distributed on the top and bottom sides of the 3D model respectively.

We first consider the case of a velocity model with one inclusion in the homogeneous background. The velocity in the inclusion is 3500 m/s (Figure 6). The inclusion is centred on the 3D grid. The 4 frequencies were inverted successively. Some horizontal and vertical sections of the inclusion are shown in Figure 6. Note the vertically-elongated shape of the inclusion in the vertical cross-section section and the symmetric shape of the inclusion in the horizontal slice. The vertically-elongated shape of the inclusion is due to the fact the top and bottom parts of the inclusion are mainly sampled by downgoing transmitted wave paths which have a limited resolution power while the shape of the inclusion in a horizontal plane is mainly controlled by reflections associated with shots and receivers located near a

same face of the 3D model. This relationship between the aperture illumination and the resolution of the imaging is also illustrated on the two graphs extracted from a vertical and horizontal section running trough the inclusion. The vertical graph exhibits a clear deficit of high wavenumber due to transmission-like reconstruction while the horizontal graph exhibits slight deficit of small wavenumbers due to reflection-like reconstruction. The symmetry of the image of the inclusion in the horizontal plane which results from the symmetry of the inclusion with respect to the acquisition geometry is an additional validation of the 3D FWI algorithm.

The second example contains two spherical inclusions (3500 m/s and 4500 m/s) corresponding to a positive and negative perturbations in the homogeneous background (Figure 7). The centre of the two inclusions lies on the same vertical plane in the middle of the grid. Aim of this test is to verify that the 3D inversion handles properly multi-scattering occurring between the two inclusions. The starting model, the frequencies involved in the inversion and the acquisition geometry are the same that for the previous example. For this case study, the 4 frequencies were inverted both successively and simultaneously (Figures 8 and 9). In both cases, the inversion successfully imaged the two inclusions.

Inclusion+interface velocity model

A more realistic example consists of a velocity-gradient layer above a homogeneous layer. An inclusion was incorporated into the velocity-gradient layer (Figure 10(a)). The minimum and maximum velocities are 3.8 and 6.0 km/s respectively. It is discretized on a $100\times100\times40$ grid with a grid spacing $h = 62.5$ m, which corresponds to a physical domain of 6.25 km x 6.25 km x 2.5 km. The grid spacing h was kept constant over the successive mono-

frequency inversions and was set according to the maximum inverted frequency. The starting model for inversion is the velocity-gradient layer extended down to the bottom of the model (Figure 10(b)). Acquisition system consists of two nested networks of $17 \times 17 = 289$ sources and receivers deployed on the surface. The distance between either two sources or receivers is 312.5 m. We sequentially inverted 5 frequencies ranging from 2 and 12 Hz. We computed 10 iterations per frequency. The final FWI velocity model is shown in Figure 11(a). A vertical graph across the inclusion extracted from the final FWI model is shown in Figure 11(b). The bottom layer is well recovered thanks to the large offset coverage allowing to quantitatively image a broad range of the layer wavelengths. The shape and amplitude of the inclusion ara incompletely recovered with respect to the expected resolution of the imaging at 12 Hz although the image of the inclusion remains clear in Figure 11(a). It may be due to the high velocity perturbation associated to the inclusion (1500 m/s with respect to the background) which makes the linearized inversion difficult. Qualitative inspection of the vertical graph also reveals a slight deficit of small (vertical) wavenumbers in the image of the inclusion and of the bottom layer (this is suggested by the negative velocity perturbations with respect to the true model). This deficit is explained by the surface acquisition geometry which illuminates the vertical components of the wavenumber vector with reflections only.

SEG/EAGE overthrust model

The 3-D SEG/EAGE overthrust model is a constant density acoustic model covering an area of 20 km x 20 km x 4.65 km (Aminzadeh et al., 1997). It is discretized with 25 m cubic cells, representing an uniform mesh of $801 \times 801 \times 187$ nodes. The minimum and maximum velocities in the overthrust model are 2.2 and 6.0 km/s respectively (Figure 12).

Overthrust model: channel target

Due to limited available computer resources, our first application was limited to a small target of the overthrust model centred on a channel. The maximum frequency involved in the inversion was 15 Hz. A horizontal slice and a vertical section of the model are shown in Figure 13. The model covers an area of 7 km x 8.8 km x 2.3 km and is discretized with a grid spacing $h = 50$ m. This leads to a $141 \times 176 \times 46$ grid. The minimum and maximum velocities are 3.3 and 6.0 km/s respectively. Acquisition system consists of 1452 sources and receivers deployed on the surface according to two nested grids of 44x33 nodes. The distance between either two sources or receivers is 200 m. We sequentially inverted 5 frequencies ranging from 5 to 15 Hz. For each frequency, we computed 7 iterations. The starting velocity model was obtained by smoothing the true model with a wavenumber filter with a cut-off wavenumber of $1./500\ m^{-1}$ (Figure 14). The final FWI model provides a low-pass version of the true model (Figure 15). In order to assess the accuracy of the FWI, we low-pass filter the true model in the time domain with a cut-off frequency of 15 Hz to roughly mimic the exact velocity model that would have been inferred by FWI. (Figure 16). Qualitative comparison between the final FWI velocity model and the low-pass filtered true model shows a good agreement between the two models. Comparison between a vertical graph extracted from the starting model, the low-pass true velocity model and the final FWI model is shown in Figure 17. The agreement is reasonably good with again a slight deficit of small wavenumbers in the FWI graph due to the surface-to-surface illumination and underestimation of velocities in the deep part of the model likely due to an insufficient number of iterations.

To perform this application, we used 60 MPI processes distributed over 15 dual core

biprocessor nodes. Each MPI process used 1.5 Gbytes of RAM (see Table 1). Seven iterations of the inversion of one frequency took approximately 45 hours. Table 1 gathers information related to running time and memory requirement for LU factorization, multi-shot resolutions (both tasks being devoted to the forward problem), gradient and diagonal Hessian computation. Running time for the resolution phase is very small (0.9 s per source) and illustrates the main advantage of frequency-domain modeling methods based on direct solvers for tomographic applications involving few thousands of source. Computation of the gradient is also negligible in the frequency domain (4 s) thanks to the summation without disk swapping over a very compact volume of data limited to few frequency components. Moreover, increasing the number of cores in the inversion would have led to a significant reduction of the computational time at the partial expense of memory saving due to memory overhead during parallel factorization (Operto et al., 2007).

Overthrust model: thrust target

We now consider the imaging of a significant target of the overthrust model which incorporates the main thrusts of the model (Figure 18). The minimum and maximum velocities are respectively 2.2 and 6.0 km/s. The model covers an area of 13.5 km x 13.5 km x 4.65 km.

Acquisition system consists of two coincident $43 \times 43 = 1849$ network of sources and receivers deployed on the surface. The distance between either two sources or receivers is 300 m. We sequentially inverted 2 frequencies: 3.5 and 5 Hz. We computed 10 iterations per frequency. For this application, we adapted the grid interval to the inverted frequency. Grid intervals were h=150 m and 100 m for the frequencies 3.5 and 5 Hz. These dicretizations

lead respectively to grids of dimension $90 \times 90 \times 32$ and $135 \times 135 \times 47$. The starting velocity model was obtained by smoothing the true model with a 3D Gaussian function with a correlation length of 500 meters in the 3 directions (Figure 19). The FWI velocity models after inversion of the 3.5-Hz and 5-Hz frequencies are shown in figures 20 and 21 respectively. Although the velocity structure is well imaged at a resolution scale consistent with the inverted frequencies, one can note a checkerboard pattern superimposed near the ends of the horizontal slices of the FWI velocity model. This is clearly a footprint of the coarse acquisition geometry. This pattern is only observed near the end of the horizontal slice because of the non uniform azimuth illumination in these parts of the model. The acquisition footprint has no preferential orientation due to the fact that both shots and receivers are uniformally deployed all over the surface with a constant spacing in the dip and cross directions. Another illustration of the footprint of the azimuth illumination and of the acquisition coarseness on 3D frequency-domain FWI was illustrated by Sirgue et al. (2007).

For this application, we run 32 processes distributed over 8 dual core biprocessor nodes (4 MPI processes/node) for the 150-m grid (frequency 3.5 Hz) and 60 processes distributed over 20 dual core biprocessor nodes (3 MPI processes/node) for the 100-m grid (frequency 5 Hz) respectively. Note that the number of process per dual core biprocessor node was decreased from 4 to 3 as the size of the problem increases in order to increase the amount of share memory assigned to each processor for large problems. This allows optimization of the memory use at the partial expense of the running time since the memory overhead decreases with the number of process.

The 10 iterations took about 24 hours and 72 hours for the 3.5-Hz and the 5-Hz frequencies respectively. More detailed information are gathered in the table 2.

We considered that we obtained convergence when the cost function reached about 10 % of its initial value (see Figure 22). We notice that we reached a better convergence rate that shown in Figure 7a of Sirgue et al. (2007). This may be due to different scaling of the gradient or to the smaller size of our application.

The data fit is illustrated in the frequency domain for the 3.5-Hz and 5-Hz frequencies for 2 shots in Figures 23 and 24 respectively. We compare the spectral amplitude and the phase of the monochromatic wavefields at the receiver positions computed in the true velocity model and in the FWI models at the first and last iterations of the two mono-frequency inversions. One shot is located at the upper-left corner of the receiver plane (Figure 23) while the second shot is on the middle of the receiver array (Figure 24). The misfit reduction between the first and last iterations is obvious. We note also that this misfit reduction is more effective for the shot located in the middle of the receiver array illustrating the difficulty to match the lower-amplitude arrivals recorded at larger offsets.

CONCLUSION

In this paper, we presented a 3D massively parallel frequency-domain full-waveform inversion algorithm based on a direct solver. Advantages of our approach is related to the robustness of the forward problem provided by the use of a high-performance direct solver, its efficiency to perform multiple-shot simulations in 3D finite-difference grids of relatively small dimensions and a straightforward parallelization of the inverse problem resulting from a domain decomposition of the monochromatic wavefields performed by the direct solver. Its main drawback is the memory and CPU time complexity of the LU factorization phase which limits the size of the models and the frequency bandwidth which can be addressed on realistic distributed-memory platforms. We presented several applications on synthetic

examples of increasing complexity to validate the algorithm and to give some insights of the feasibility of our approach. Some preliminary applications to the overthrust model suggests that frequency-domain FWI can be successfully applied at low frequencies (< 5 Hz) on limited-size PC clusters to develop 3D velocity models with a maximum resolution of the order of half the wavelength (that is, 400 m for a velocity of 4000 m/s). Successfull modeling was already performed in a significant target of the overthrust model at 7 Hz (Operto et al., 2007) using 400 Gbytes of core memory suggesting that full-waveform inversion is feasible at this frequency if large computational ressources are made available. At the resolution scale provided by this range of frequencies (5-7 Hz), the velocity models may be used as improved background models for prestack depth migration.

Aim of our future work is to overcome the memory limitations imposed by the use of a direct solver only. A possible way is to evolve towards hybrid direct-iterative solvers implemented in a domain decomposition method for which the direct solver is applied to subdomains of limited dimension while the iterative solver is applied to the grid points located at the boundaries between the subdomains. The relevance of this approach will have to be demonstrated when a large number of sources is considered.

Analysis of the sensitivity of FWI to the acquisition geometry and to the accuracy of the starting model needs further investigations before being able to move to 3D real data applications.

ACKNOWLEDGEMENTS

Access to the high performance computing facilities of MESOCENTRE SIGAMM computer center provided the required computer resources and we gratefully acknowledge both this

facility and the support of the staff. We are particularly grateful to A. Miniussi for his help during the installation of the software on the cluster. Finally, this work was carried out within the frame of the SEISCOPE consortium (http://geoazur.unice.fr/SEISCOPE) sponsored by BP, CGG-Veritas, EXXON-Mobil, TOTAL and SHELL.

$MEM_{FACTO_{ALL}}$ $(GBytes)$	67
$MEM_{FACTO_{PROC}}$ $(GBytes)$	1.5
$TIME_{FACTO}$ (s)	510
$TIME_{SOLVE_{ALL}}$ (s)	1270
$TIME_{SOLVE_{SOURCE}}$ (s)	0.9
$TIME_{GRADIENT}$ (s)	4
$TIME_{diag_{HESSIAN_a}}$ (s)	3093

Table 1: Computational cost of the imaging of the overthrust model (channel): $MEM_{FACTO_{ALL}}$: Total memory allocated during factorization. $MEM_{FACTO_{PROC}}$: Average allocated memory per working processor during factorization. $TIME_{FACTO}$: Elapsed time for factorization. $TIME_{SOLVE_{ALL}}$: Total elapsed time for multi-shot resolution. $TIME_{SOLVE_{SOURCE}}$: Elapsed time for resolution for 1 source. $TIME_{GRADIENT}$: Elapsed time for gradient computation. $TIME_{diag_{HESSIAN_a}}$: Elapsed time for diagonal Hessian computation.

$FREQUENCY\ (Hz)$	3.5	5
$GRID$	$90 \times 90 \times 32$	$135 \times 135 \times 47$
$MEM_{FACTO_{ALL}}\ (GBytes)$	16	64
$MEM_{FACTO_{PROC}}\ (GBytes)$	0.4	1.1
$TIME_{FACTO}\ (s)$	72	340
$TIME_{SOLVE_{ALL}}\ (s)$	310	995
$TIME_{SOLVE_{SOURCE}}\ (s)$	0.165	0.53
$TIME_{GRADIENT}\ (s)$	0.65	1.44
$TIME_{diag_{HESSIAN_a}}\ (s)$	1999	3432

Table 2: Computational cost of the imaging of the overthrust model (thrust system): $FREQUENCY$: inverted frequency. $GRID$: dimension of the 3D FD grid. $MEM_{FACTO_{ALL}}$: Total memory allocated during factorization. $MEM_{FACTO_{PROC}}$: Average allocated memory per working processor during factorization. $TIME_{FACTO}$: Elapsed time for factorization. $TIME_{SOLVE_{ALL}}$: Total elapsed time for multi-shot resolution. $TIME_{SOLVE_{SOURCE}}$: Elapsed time for resolution of 1 source. $TIME_{GRADIENT}$: Elapsed time for gradient computation. $TIME_{diag_{HESSIAN_a}}$: Elapsed time for diagonal Hessian computation.

REFERENCES

Amestoy, P. R., I. S. Duff, J. Y. L'Excellent, and J. Koster, 2007, Multifrontal massively parallel solver (MUMPS version 4.6): Users'guide. http://enseeiht.fr/apo/MUMPS/ and http://graal.ens-lyon.fr/MUMPS/.

Amestoy, P. R., A. Guermouche, J. Y. L'Excellent, and S. Pralet, 2006, Hybrid scheduling for the parallel solution of linear systems: Parallel computing, **32**, 136–156.

Aminzadeh, F., J. Brac, and T. Kunz, 1997, 3-D Salt and Overthrust models: Society of Exploration Geophysicists.

Ben-Hadj-Ali, H., S. Operto, J. Virieux, and F. Sourbier, 2007, 3D acoustic frequency-domain full-waveform inversion: 77^{th} SEG Annual Meeting (San Antonio, 23-28 September), Expanded Abstracts, 1730–1734, Society of Exploration Geophysicists.

Berenger, J.-P., 1994, A perfectly matched layer for absorption of electromagnetic waves: Journal of Computational Physics, **114**, 185–200.

Brenders, A. J. and R. G. Pratt, 2006a, Efficient waveform tomography for lithospheric imaging: implications for realistic 2D acquisition geometries and low frequency data: Geophysical Journal International.

———, 2006b, Full waveform tomography for lithospheric imaging: results from a blind test in a realistic crustal model: Geophysical Journal International.

Chauris, H., M. Noble, G. Lambaré, and P. Podvin, 2002, Migration velocity analysis from locally coherent events in 2d laterally heterogeneous media, part 1: Theoretical aspects: Geophysics, **67**, 1202–1212.

Clarke, R., G. Xia, N. Kabir, L. Sirgue, and S. Michell, 2007, Processing of a novel deep-water, wide-azimuth node seismic survey: The leading edge, **April**, 504–509.

Duff, I. S. and J. K. Reid, 1983, The multifrontal solution of indefinite sparse symmetric

linear systems: ACM Transactions on Mathematical Software, **9**, 302–325.

Hicks, G. J. and R. G. Pratt, 2001, Reflection waveform inversion using local descent methods: estimating attenuation and velocity over a gas-sand deposit: Geophysics, **66**, 598–612.

Hustedt, B., S. Operto, and J. Virieux, 2004, Mixed-grid and staggered-grid finite difference methods for frequency domain acoustic wave modelling: Geophysical Journal International, **157**, 1269–1296.

Jo, C. H., C. Shin, and J. H. Suh, 1996, An optimal 9-point, finite-difference, frequency-space 2D scalar extrapolator: Geophysics, **61**, 529–537.

Marfurt, K., 1984, Accuracy of finite-difference and finite-elements modeling of the scalar and elastic wave equation: Geophysics, **49**, 533–549.

Operto, S., G. Lambaré, P. Podvin, and P. Thierry, 2003, 3-D ray-Born migration/inversion. part 2: application to the SEG/EAGE overthrust experiment: Geophysics, **68**, 1357–1370.

Operto, S., C. Ravaut, L. Improta, J. Virieux, A. Herrero, and P. Dell'Aversana, 2004, Quantitative imaging of complex structures from multi-fold wide aperture seismic data: Geophysical Prospecting, **52**, 625–651.

Operto, S., J. Virieux, P. Amestoy, J.-Y. L'Éxcellent, L. Giraud, and H. Ben-Hadj-Ali, 2007, 3D finite-difference frequency-domain modeling of visco-acoustic wave propagation using a massively parallel direct solver: A feasibility study: Geophysics, **72**, SM195–SM211.

Operto, S., J. Virieux, J. X. Dessa, and G. Pascal, 2006, Crustal imaging from multifold ocean bottom seismometers data by frequency-domain full-waveform tomography: application to the eastern nankai trough: Journal of Geophysical Research, **111**, doi:10.1029/2005JB003835.

Operto, S., J. Virieux, and A. Ribodetti, 2005, Multiple arrival migration/inversion of real global aperture seismic data: 67^{th} Annual EAGE Conference and Exhibition, Expanded Abstracts, P272, EAGE.

Operto, S., S. Xu, and G. Lambaré, 2000, Can we image quantitatively complex models with rays?: Geophysics, **65**, 1223–1238.

Plessix, R. E., 2007, A helmholtz iterative solver for 3d seismic-imaging problems: Geophysics, **72**, SM185–SM194.

Pratt, R. G., 1999, Seismic waveform inversion in the frequency domain, part I : theory and verification in a physic scale model: Geophysics, **64**, 888–901.

———, 2004, Velocity models from frequency-domain waveform tomography: past, present and future: Presented at the 66^{th} Annual EAEG Meeting, Paris, Eur. Ass. Expl. Geophys.

Pratt, R. G., C. Shin, and G. J. Hicks, 1998, Gauss-newton and full newton methods in frequency-space seismic waveform inversion: Geophysical Journal International, **133**, 341–362.

Pratt, R. G. and P. Williamson, 1990, Inverse theory applied to multi-source cross-hole tomography. part 1 : acoustic wave-equation method.: Geophysical Prospecting, **38**, 287–310.

Ravaut, C., S. Operto, L. Improta, J. Virieux, A. Herrero, and P. dell'Aversana, 2004, Multi-scale imaging of complex structures from multi-fold wide-aperture seismic data by frequency-domain full-wavefield inversions: application to a thrust belt: Geophysical Journal International, **159**, 1032–1056.

Riyanti, C. D., A. Kononov, Y. A. Erlangga, C. Vuik, C. Oosterlee, R. E. Plessix, and W. A. Mulder, 2007, A parallel multigrid-based preconditioner for the 3d heterogeneous high-frequency helmholtz equation: Journal of Computational physics, **224**, 431–448.

Shin, C., K. Yoon, K. J. Marfurt, K. Park, D. Yang, H. Y. Lim, S. Chung, and S. Shin, 2001, Efficient calculation of a partial derivative wavefield using reciprocity for seismic imaging and inversion: Geophysics, **66**, 1856–1863.

Shipp, R. M. and S. C. Singh, 2002, Two-dimensional full wavefield inversion of wide-aperture marine seismic streamer data: Geophysical Journal International, **151**, 325–344.

Sirgue, L., J. Etgen, and U. Albertin, 2007, 3D full waveform inversion: Wide versus narrow azimuth acquisitions: 77^{th} SEG Annual Meeting (San Antonio, 23-28 September), Expanded Abstracts, 1760–1764, Society of Exploration Geophysicists.

Sirgue, L. and R. G. Pratt, 2004, Efficient waveform inversion and imaging : a strategy for selecting temporal frequencies: Geophysics, **69**, 231–248.

Stekl, I. and R. G. Pratt, 1998, Accurate viscoelastic modeling by frequency-domain finite difference using rotated operators: Geophysics, **63**, 1779–1794.

Stekl, I., M. R. Warner, and A. P. Umpleby, 2007, 3D frequency domain waveform inversion - synthetic shallow channel example: EAGE 69th Conference and exhibition, Expanded Abstracts, C026, EAGE.

Stork, C., 1992, Reflection tomography in the post migrated domain: Geophysics, **57**, 680–692.

Tarantola, A., 1987, Inverse problem theory: methods for data fitting and model parameter estimation: Elsevier.

Warner, M., I. Stekl, and A. Umpleby, 2007, Full wavefield seismoc tomography - iterative forward modelling in 3d: 69th EAGE Conference and Exhibition incorporating SPE EUROPEC 2007 ,London, Expanded Abstracts, C025, EAGE.

Wu, R.-S. and M. N. Töksoz, 1987, Diffraction tomography and multisource holography applied to seismic imaging: Geophysics, **52**, 11–25.

Yilmaz, Ö. and R. Chambers, 1984, Migration velocity analysis by wavefield extrapolation: Geophysics, **49**, 1664–1674.

Zhang, Y., S. Xu, and G. Zhang, 2006, Imaging complex salt bodies with turning-wave one-way wave equation: 76th annual meeting, Expanded Abstracts, 2323–2327, Soc. Expl. Geophys.

Zhang, Y., G. Zhang, D. Yingst, and J. Sun, 2007, Explicit marching method for reverse-time migration: 77th annual meeting, Expanded Abstracts, 2300–2304, Soc. Expl. Geophys.

LIST OF FIGURES

8 Imaging of 2 inclusions by 3D FWI: vertical cross-sections of the FWI velocity models after successive inversion of frequencies 1.75 (a), 2.35 (b), 3.00 (c) and 3.75 (d) Hz.

9 Imaging of 2 inclusions by 3D FWI: vertical cross-section of the 3D FWI velocity model after simultaneous inversion of the 4 frequencies 1.75, 2.35, 3.00 and 3.75 Hz.

10 Imaging of the inclusion/interface model: (a) True velocity model. (b) Starting velocity model for FWI.

11 Imaging of the inclusion/interface model: (a) Final FWI velocity model. (b) Vertical graph across the inclusion extracted from the FWI velocity model (red) and from the true velocity model (black).

12 The 3D SEG/EAGE overthrust model.

13 Imaging of a channel in the overthrust model: true velocity model. a) Horizontal slice at z=1.5 km. b) Cross-section at x=4 km.

14 Imaging of a channel in the overthrust model: starting velocity model. a) Horizontal slice at Z=1.5 km. b) Cross-section at X=4 km.

15 Imaging of a channel in the overthrust model: FWI velocity model after successive inversion of the 5 frequencies. a) Horizontal slice at z=1.5 km. b) Vertical section at x=4 km.

16 Imaging of a channel in the overthrust model: low-pass filtered true velocity model. a) Horizontal slice at Z=1.5 km. b) Cross-section at X=4 km.

17 Imaging of a channel in the overthrust model: comparison between vertical graphs extracted from the starting model (red dashed line), the low-pass filtered true model (blue solid line) and the final FWI velocity model (black dot line). The graph is located at $(X = 3.5 \text{ km}, Y = 4.4 \text{ km})$.

18 Imaging of the thrust system in the overthrust model: true velocity model. a)

Horizontal slice at Z=2.3 km. b) Cross-section at X=6.75 km.

19 Imaging of the thrust system in the overthrust model: starting velocity model. a) Horizontal slice at Z=2.3 km. b) Cross-section at X=6.75 km.

20 Imaging of the thrust system in the overthrust model: 3.5-Hz FWI velocity model. a) Horizontal slice at Z=2.3 km. b) Cross-section at X=6.75 km.

21 Imaging of the thrust system in the overthrust model: 5-Hz FWI velocity model. a) Horizontal slice at Z=2.3 km. b) Cross-section at X=6.75 km.

22 Imaging of the thrust system in the overthrust model: cost function versus iteration number for the 3.5-Hz and 5-Hz frequencies.

23 Imaging of the thrust system in the overthrust model: a) samplitude (left) and phase (right) of the 3.5-Hz monochromatic wavefield computed in the true velocity model at the receiver positions. The horizontal and vertical axis label the receiver number in the dip and cross directions respectively. The source is located in the upper-left corner of the receiver array. b) same than (a) but the wavefields were computed in the starting model of the 3.5-Hz inversion. c) Difference between maps shown in a) and b). d) Same than (a) but the wavefields were computed in the final model of the 3.5-Hz inversion. e) Difference between maps shown in (a) and (d). (f-j): same that for (a-e) but for the 5-Hz frequency.

24 Imaging of the thrust system in the overthrust model: Same that for Figure 23 but for a source located in the middle of the receiver array.

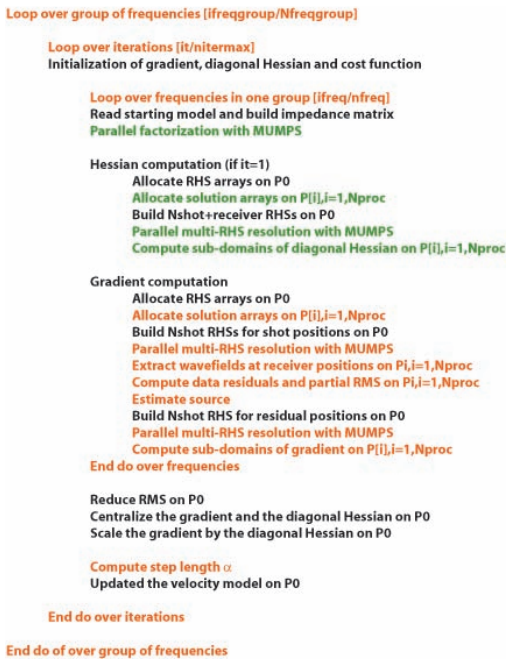

Figure 1: Sketch of the FWI algorithm. Tasks performed in parallel are written in green. RHS stands for right-hand side terms and correspond to sources in the frame of full-waveform modeling. $Nproc$ stands for the number of processes involved in the parallel execution. P_i stands for the processor i where P_0 is the master processor. Note that an arbitrary number N of frequencies can be inverted simultaneously (set $Nfreqgroup = 1$ and $nfreq = N$) or successively (set $Nfreqgroup = N$ and $nfreq = 1$). $nitermax$ stands for the maximum number of iterations of one frequency group inversion.

Ben Hadj Ali & al –

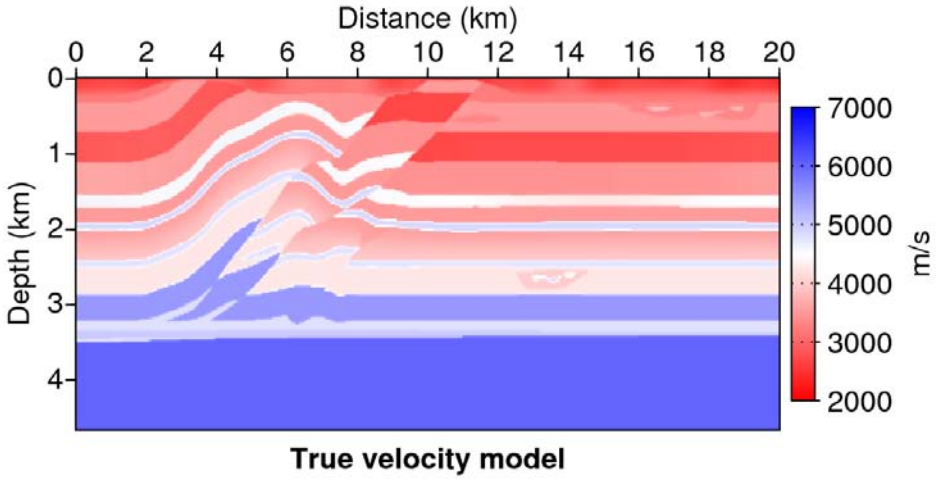

(a)

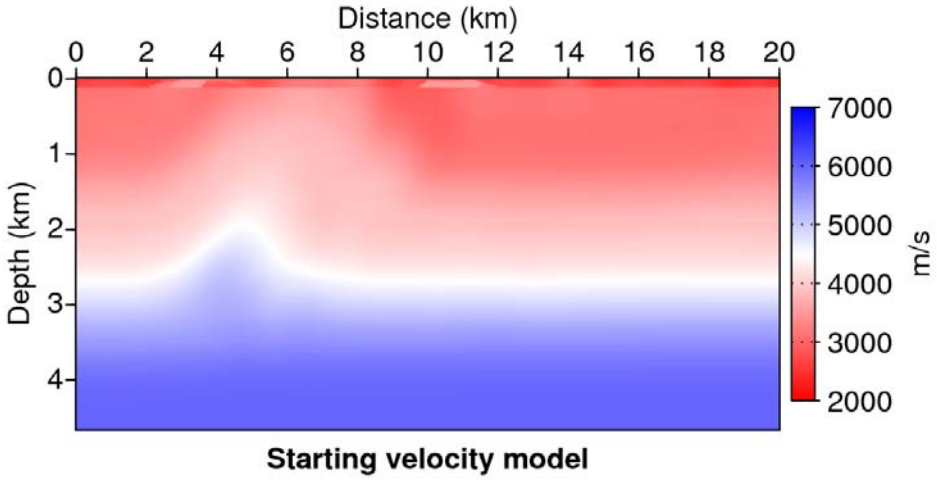

(b)

Figure 2: Imaging of a dip section of the overthrust model: a) True velocity model. b) Starting velocity model.

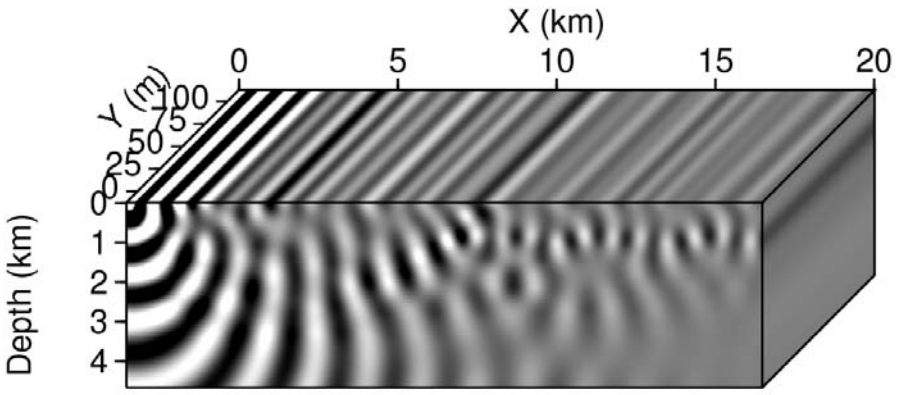

Figure 3: Example of a 2-D wavefield computed in a 3D FD grid. Note the limited dimension of the grid in the y dimension. Five grid points are used in the y direction.

Ben Hadj Ali & al –

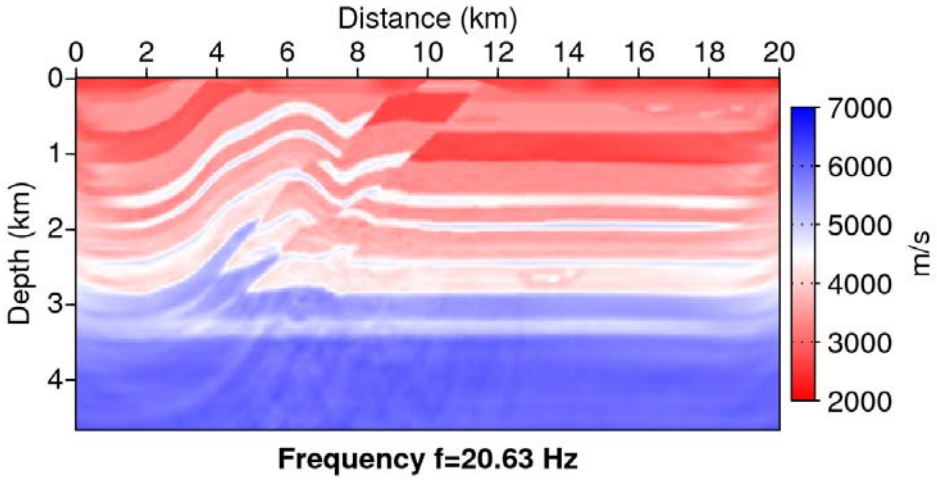

(a)

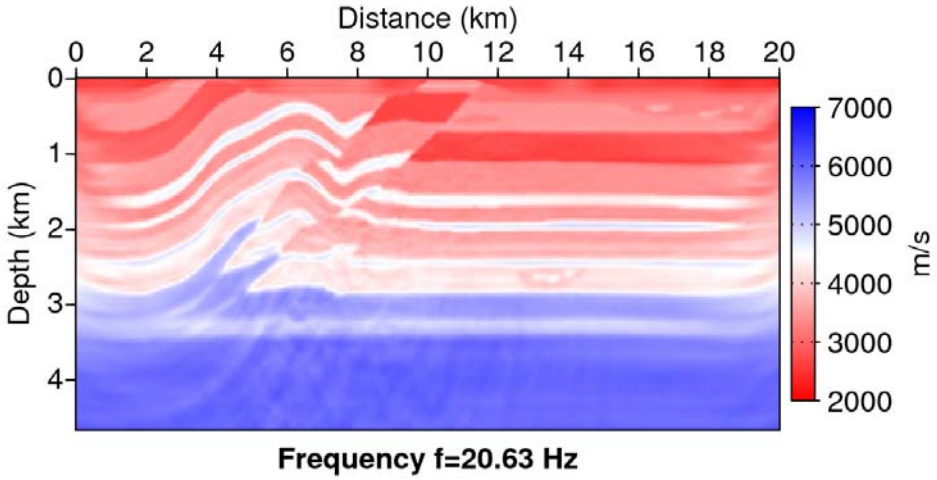

(b)

Figure 4: Imaging of a dip section of the overthrust model: (a) Final velocity model from 2D FWI. (b) Final velocity model from 3D FWI.

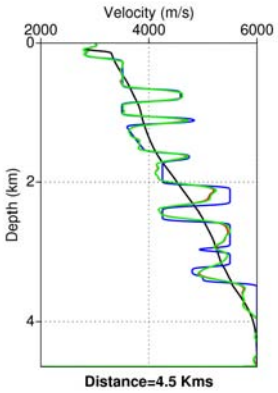

(a)

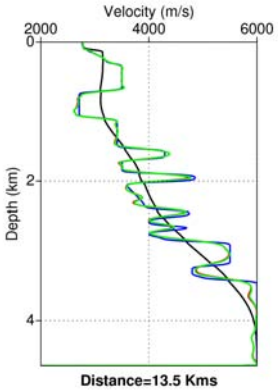

(b)

Figure 5: Imaging of a dip section of the overthrust model: Comparison between vertical graphs extracted from the true (blue line), the starting (black line) and the 2D and 3D FWI models (red and green lines respectively). The two series of graph are located at 4.5 and 13.5 km of distance. The 2D and 3D FWI graphs are almost identical.

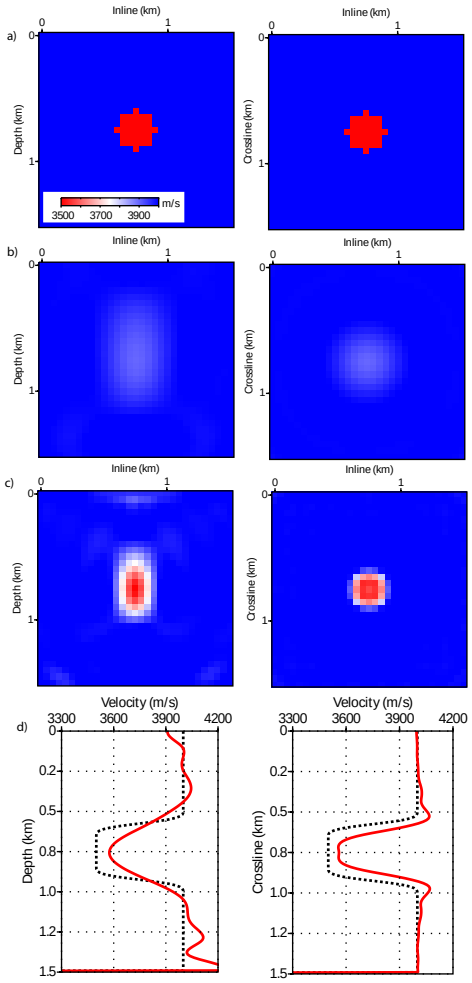

Figure 6: Imaging of 1 inclusion by 3D FWI. a) vertical (left) and horizontal (right) sections of the true inclusion. b) vertical (left) and horizontal (right) sections of the inclusion after inversion of the 1.75-Hz frequency. c) vertical (left) and horizontal (right) sections of the inclusion after inversion of the 3.75-Hz frequency. d) vertical (left) and horizontal (right) graphs extracted from models shown in (a) (black lines) and (c) (red lines).

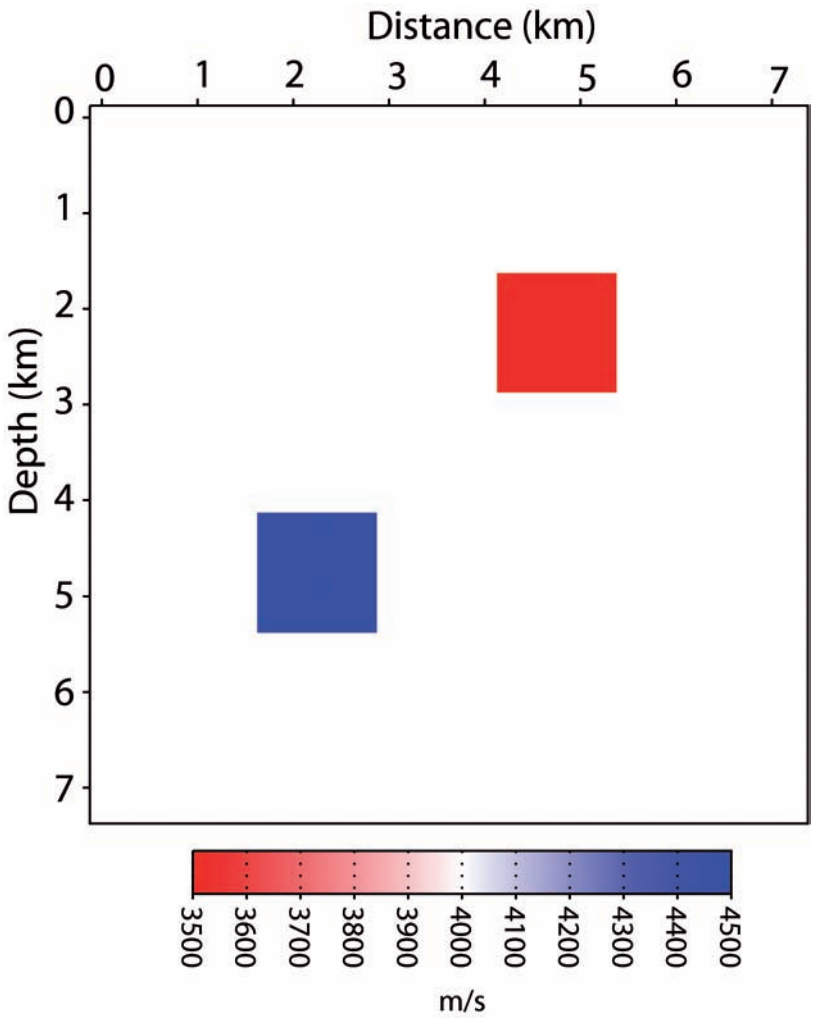

Figure 7: Imaging of 2 inclusions by 3D FWI: true model.**Ben Hadj Ali & al** –

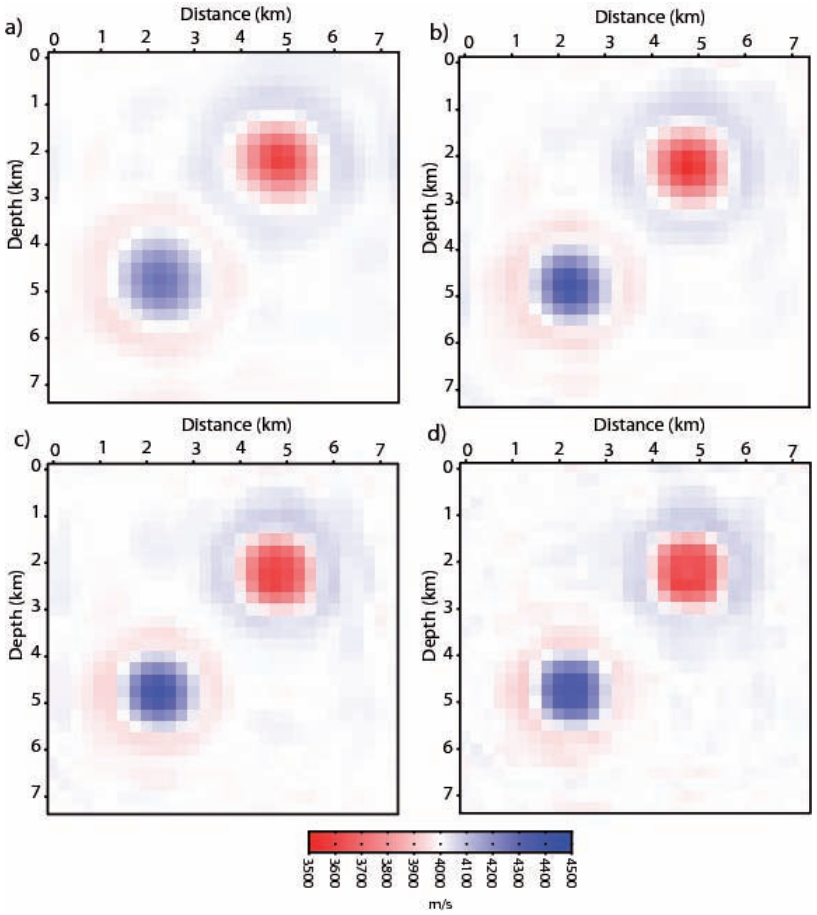

Figure 8: Imaging of 2 inclusions by 3D FWI: vertical cross-sections of the FWI velocity models after successive inversion of frequencies 1.75 (a), 2.35 (b), 3.00 (c) and 3.75 (d) Hz.

Ben Hadj Ali & al –

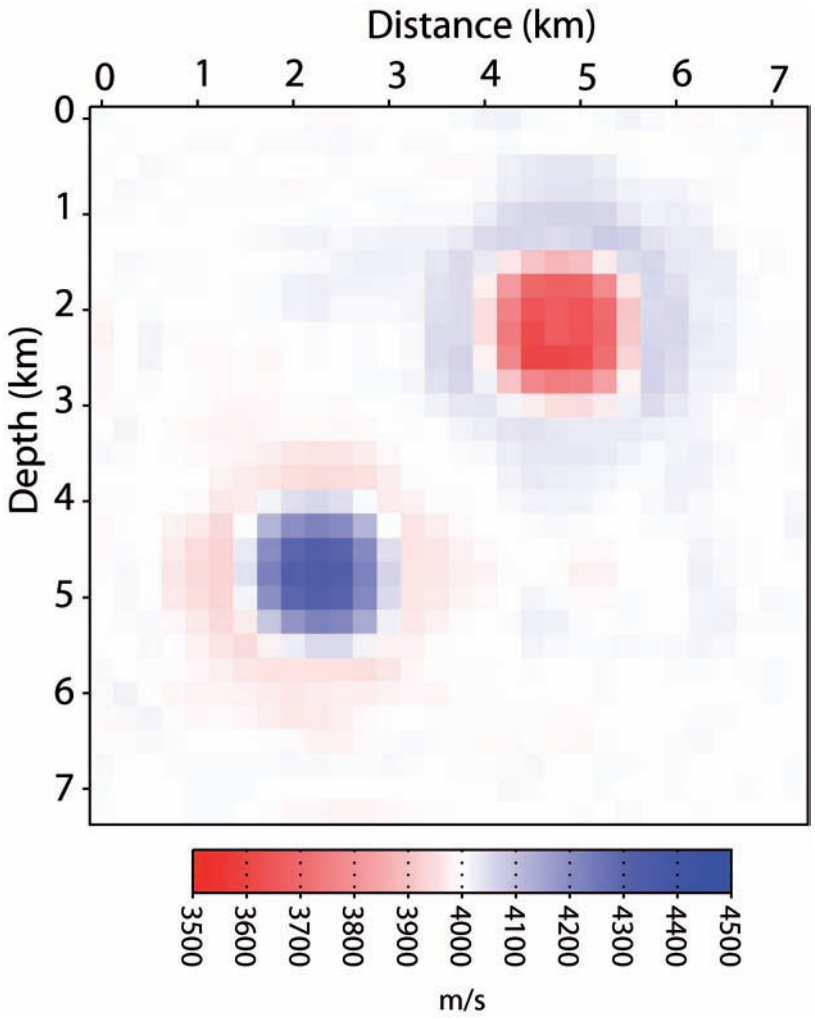

Figure 9: Imaging of 2 inclusions by 3D FWI: vertical cross-section of the 3D FWI velocity model after simultaneous inversion of the 4 frequencies 1.75, 2.35, 3.00 and 3.75 Hz.

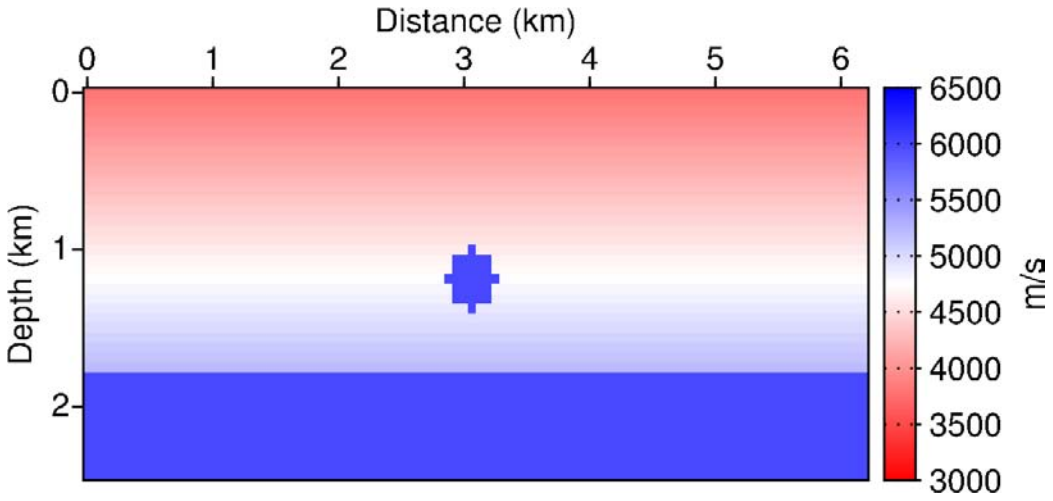

(a)

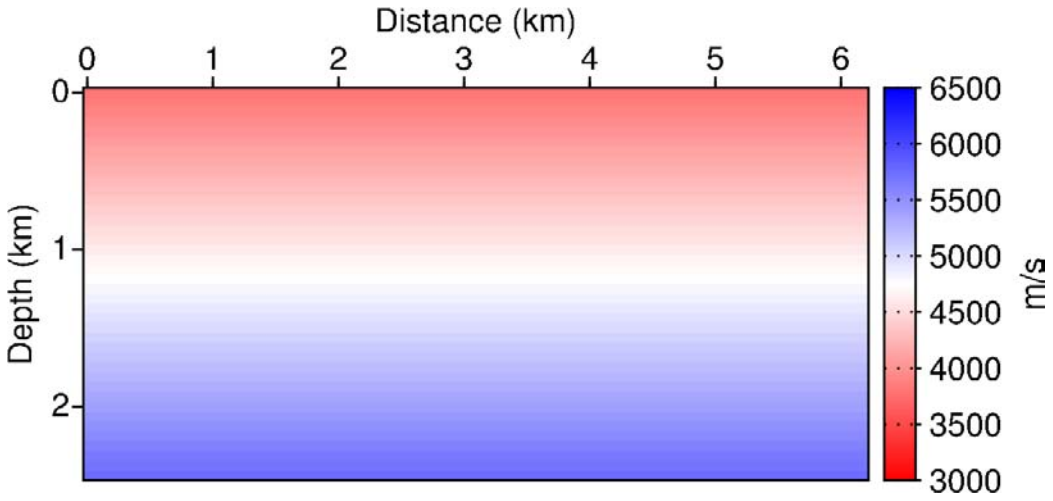

(b)

Figure 10: Imaging of the inclusion/interface model: (a) True velocity model. (b) Starting velocity model for FWI.

Ben Hadj Ali & al –

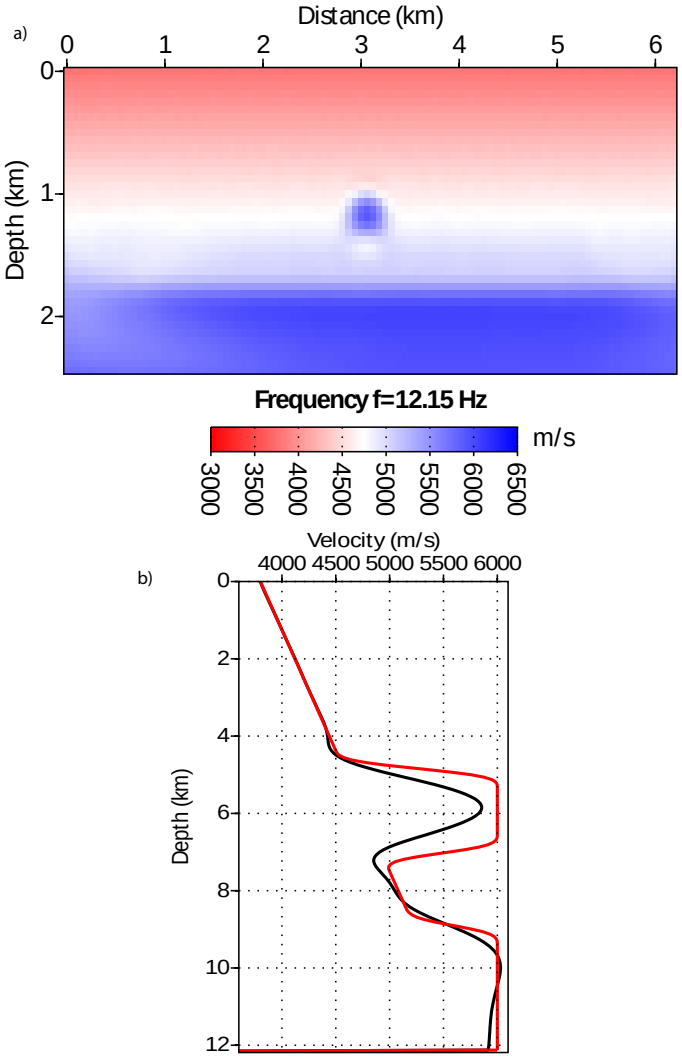

Figure 11: Imaging of the inclusion/interface model: (a) Final FWI velocity model. (b) Vertical graph across the inclusion extracted from the FWI velocity model (red) and from the true velocity model (black).

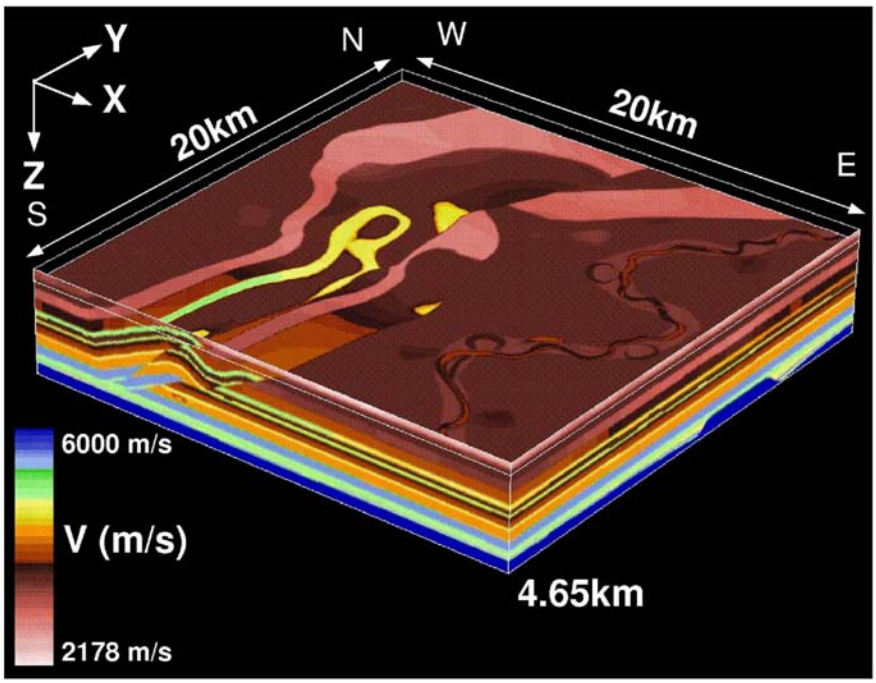

Figure 12: The 3D SEG/EAGE overthrust model.**Ben Hadj Ali & al** –

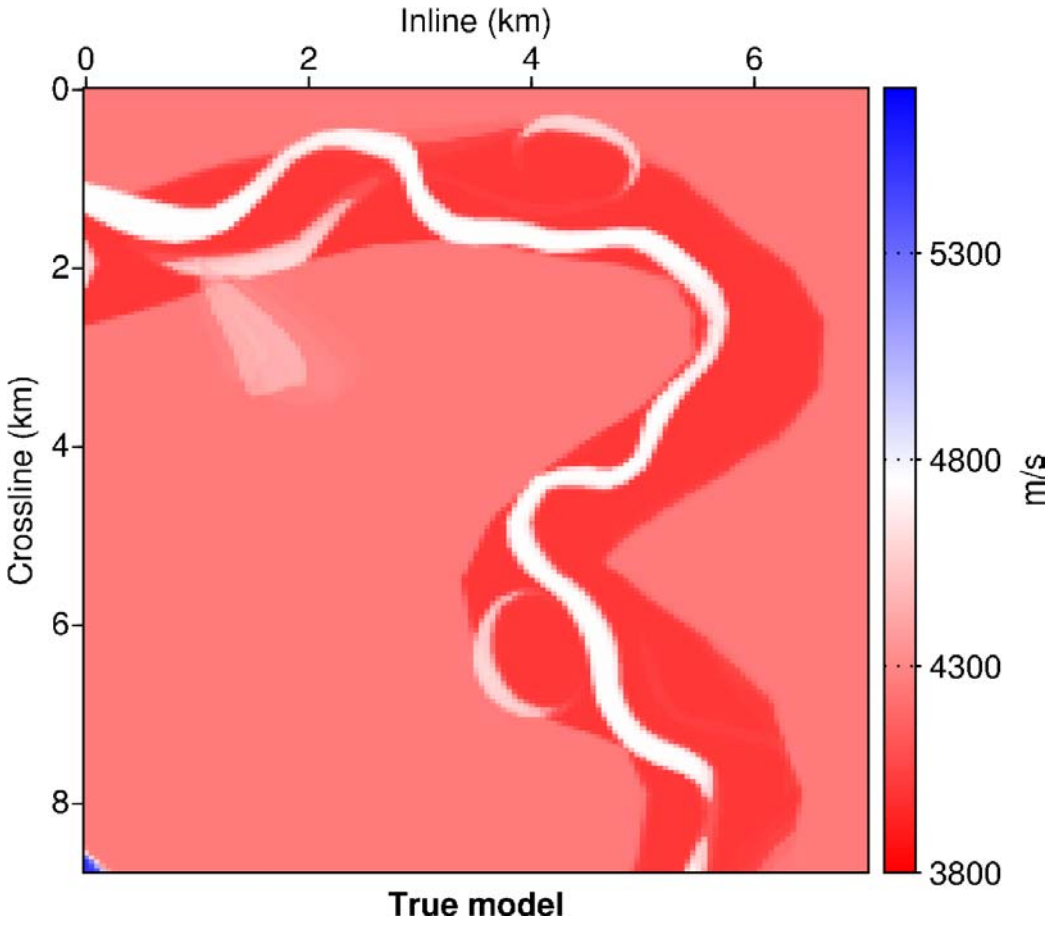

(a)

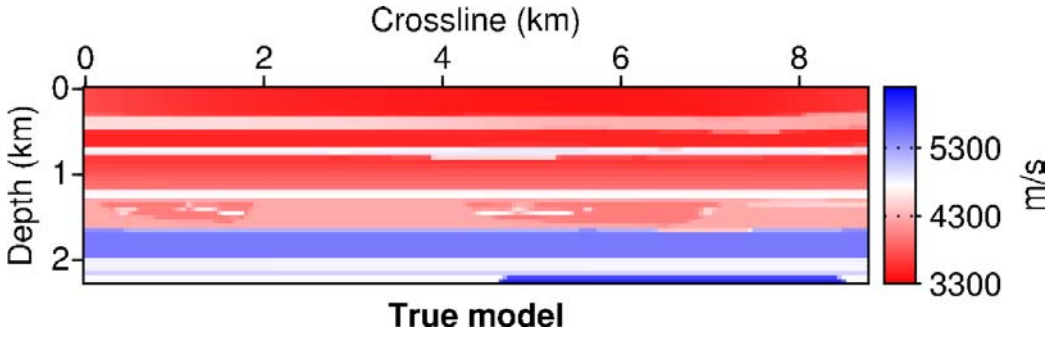

(b)

Figure 13: Imaging of a channel in the overthrust model: true velocity model. a) Horizontal slice at z=1.5 km. b) Cross-section at x=4 km.

Ben Hadj Ali & al –

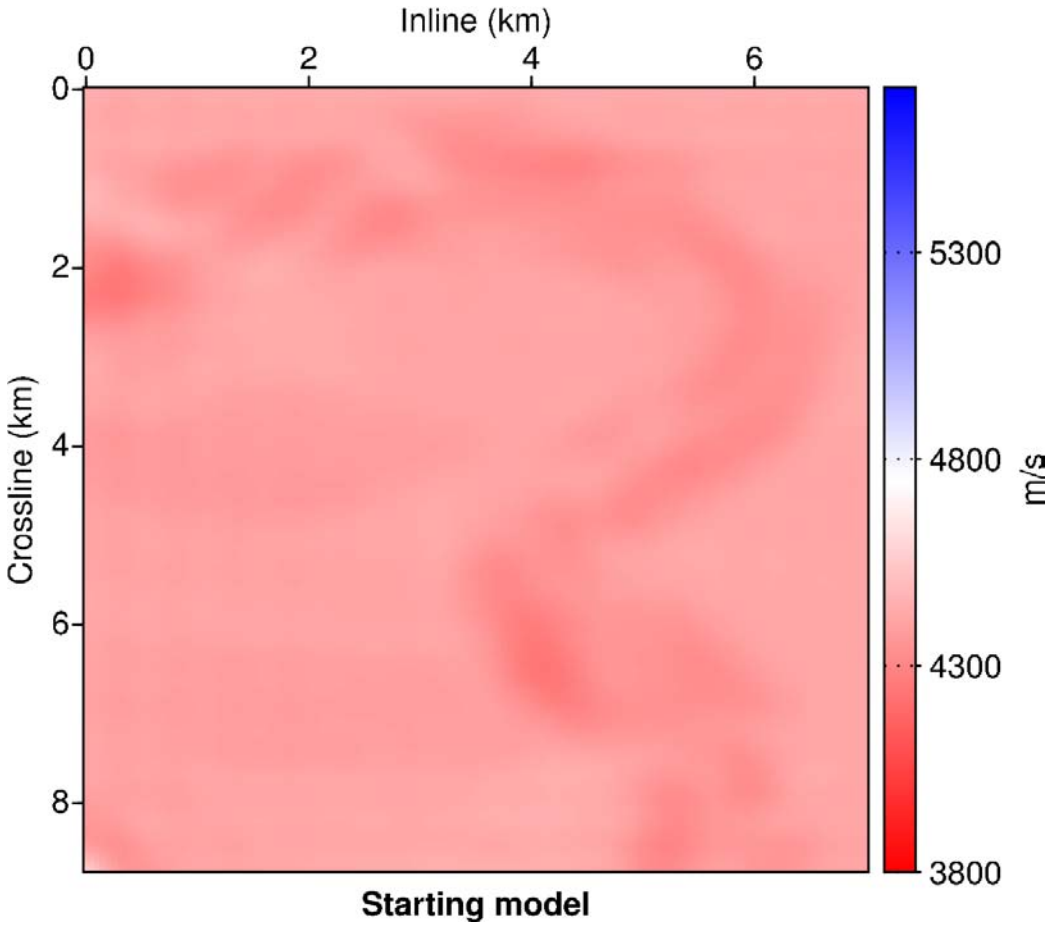

(a)

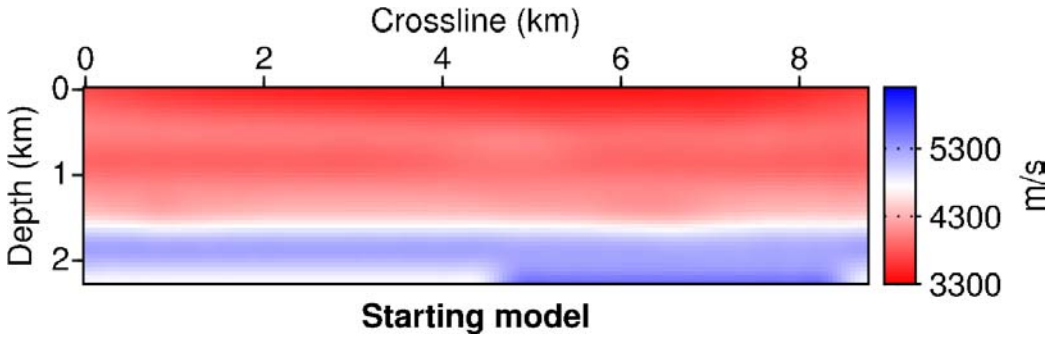

(b)

Figure 14: Imaging of a channel in the overthrust model: starting velocity model. a) Horizontal slice at Z=1.5 km. b) Cross-section at X=4 km.

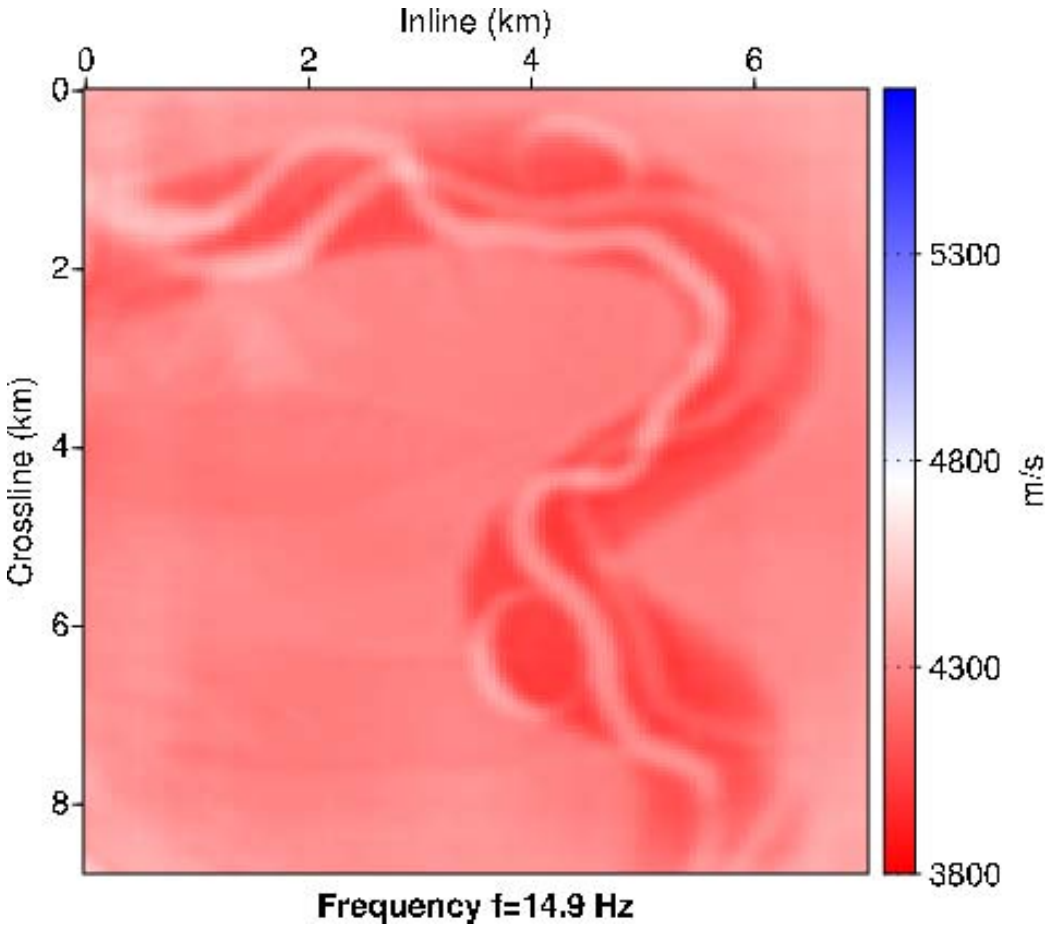

(a)

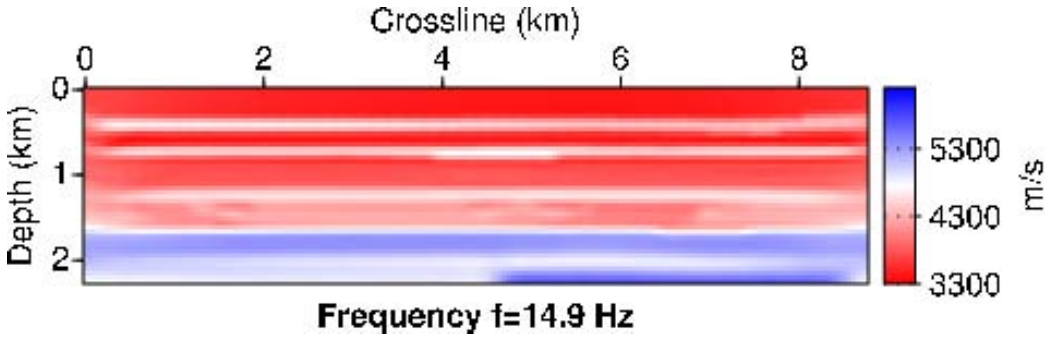

(b)

Figure 15: Imaging of a channel in the overthrust model: FWI velocity model after successive inversion of the 5 frequencies. a) Horizontal slice at z=1.5 km. b) Vertical section at x=4 km.

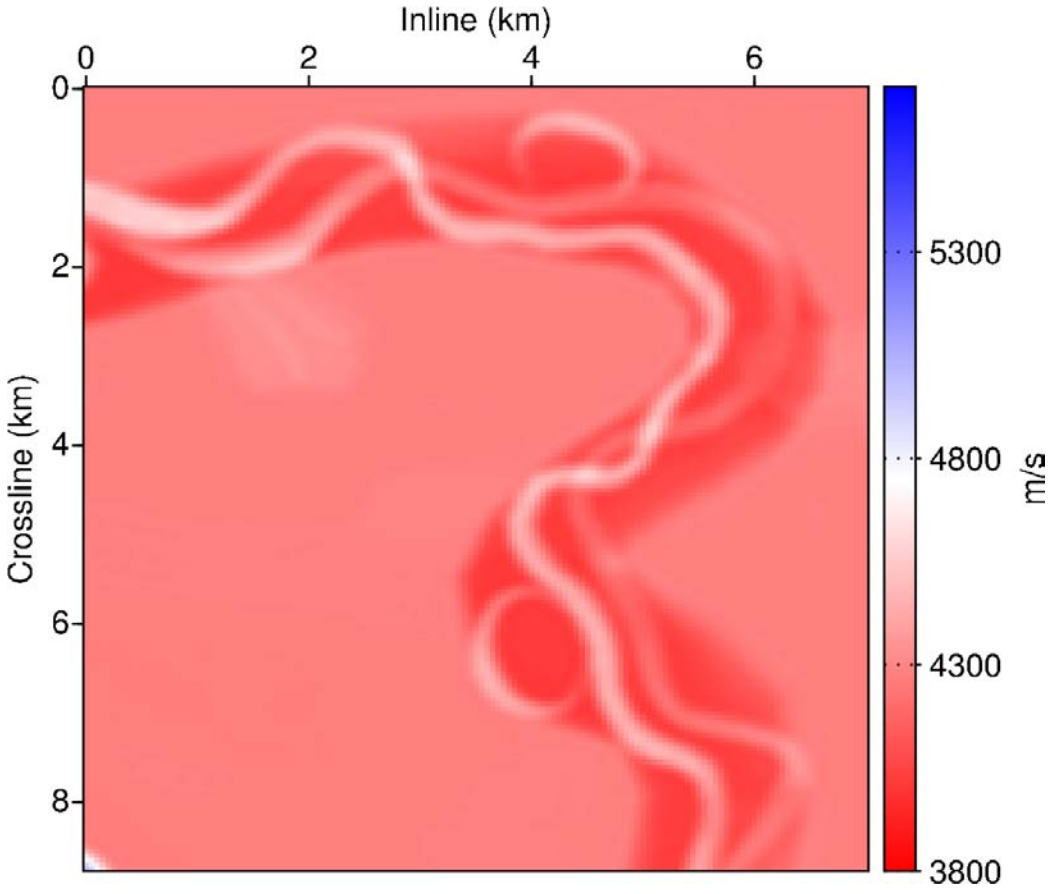

(a)

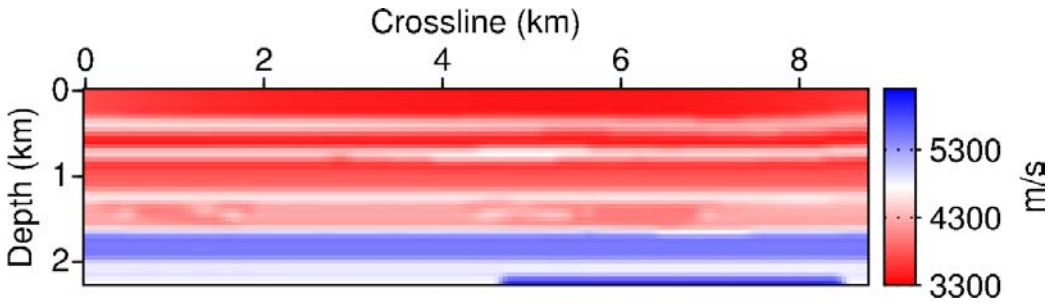

(b)

Figure 16: Imaging of a channel in the overthrust model: low-pass filtered true velocity model. a) Horizontal slice at Z=1.5 km. b) Cross-section at X=4 km.

Ben Hadj Ali & al –

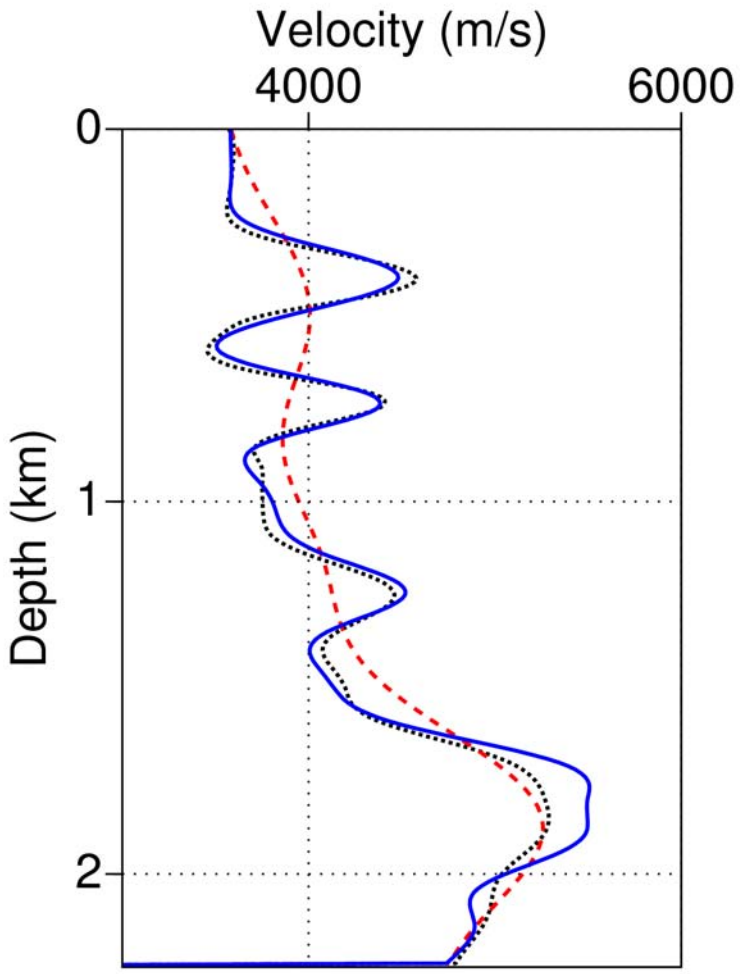

Figure 17: Imaging of a channel in the overthrust model: comparison between vertical graphs extracted from the starting model (red dashed line), the low-pass filtered true model (blue solid line) and the final FWI velocity model (black dot line). The graph is located at $(X = 3.5 \text{ km}, Y = 4.4 \text{ km})$.

Ben Hadj Ali & al –

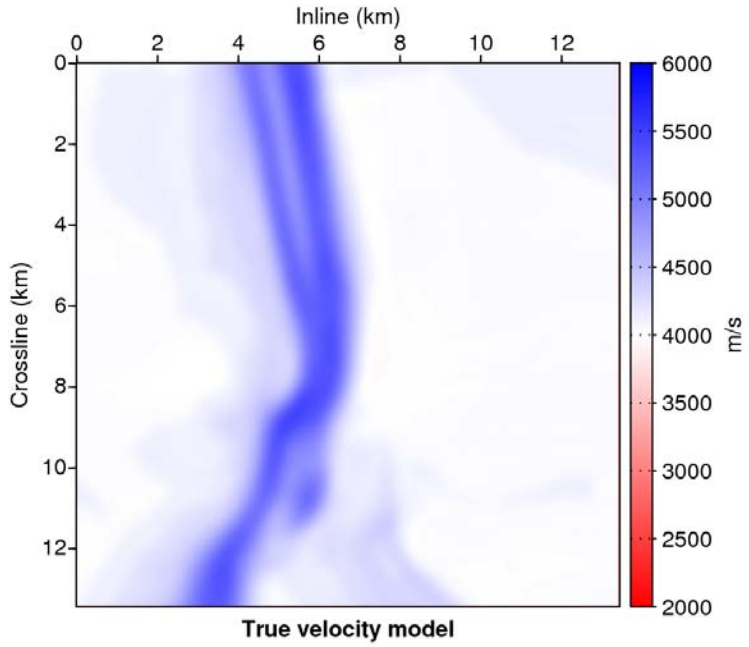

(a)

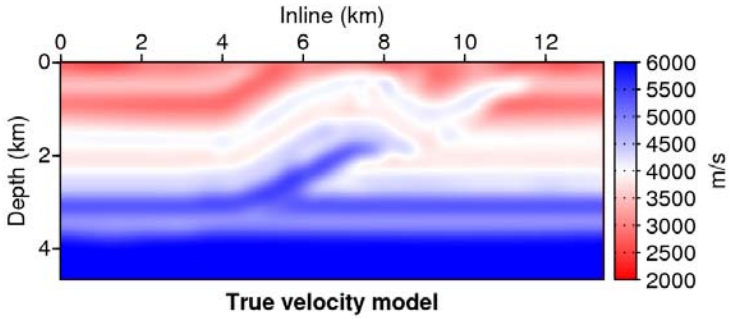

(b)

Figure 18: Imaging of the thrust system in the overthrust model: true velocity model. a) Horizontal slice at Z=2.3 km. b) Cross-section at X=6.75 km.

Ben Hadj Ali & al –

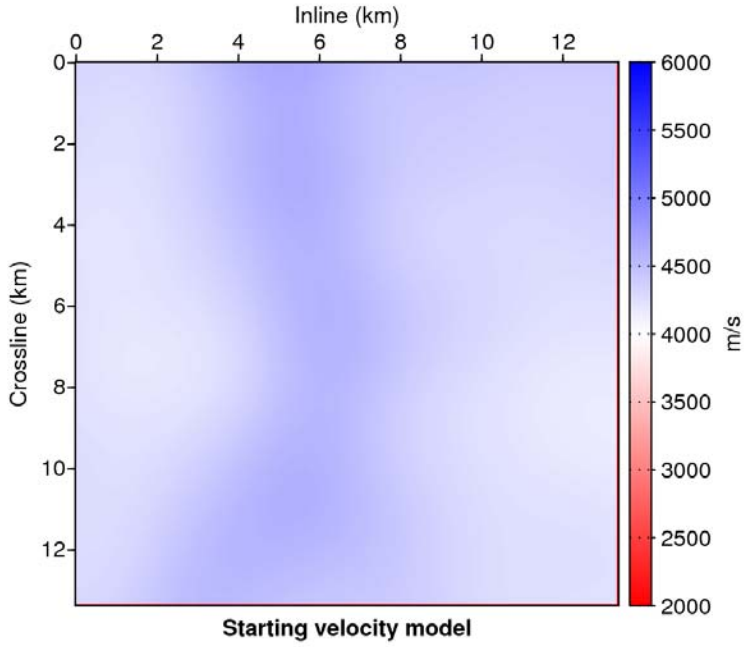

(a)

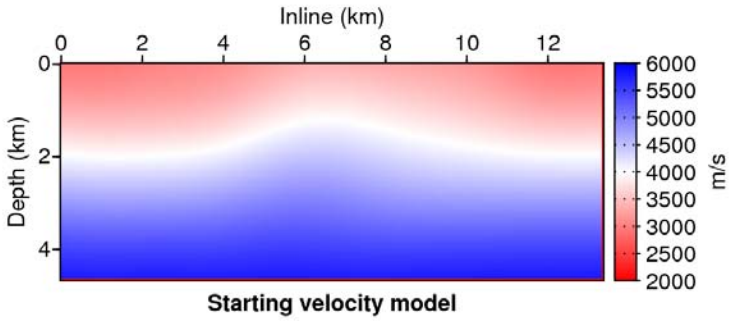

(b)

Figure 19: Imaging of the thrust system in the overthrust model: starting velocity model. a) Horizontal slice at Z=2.3 km. b) Cross-section at X=6.75 km.

Ben Hadj Ali & al –

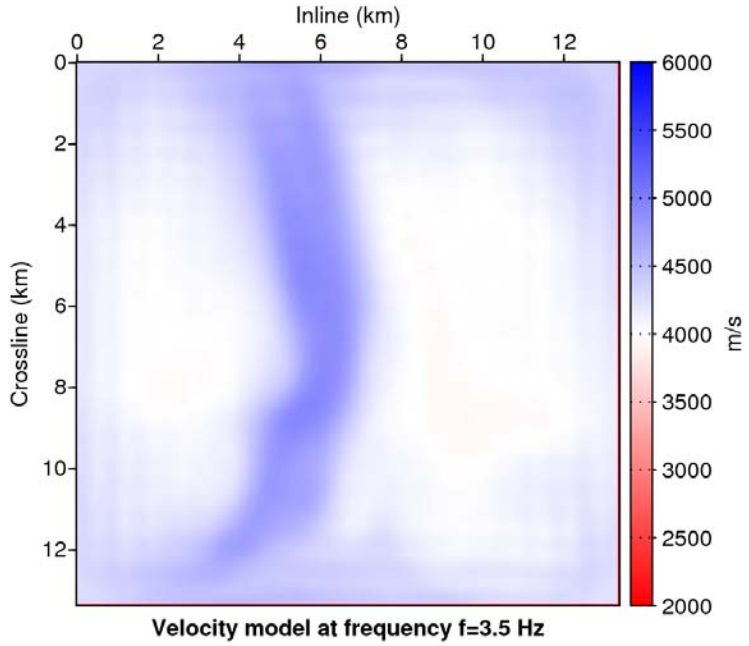

(a)

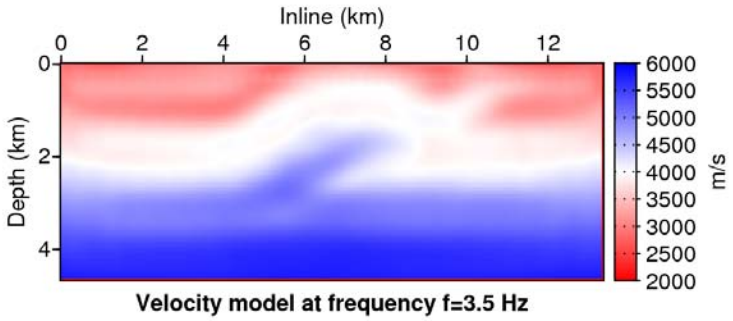

(b)

Figure 20: Imaging of the thrust system in the overthrust model: 3.5-Hz FWI velocity model. a) Horizontal slice at Z=2.3 km. b) Cross-section at X=6.75 km.

Ben Hadj Ali & al –

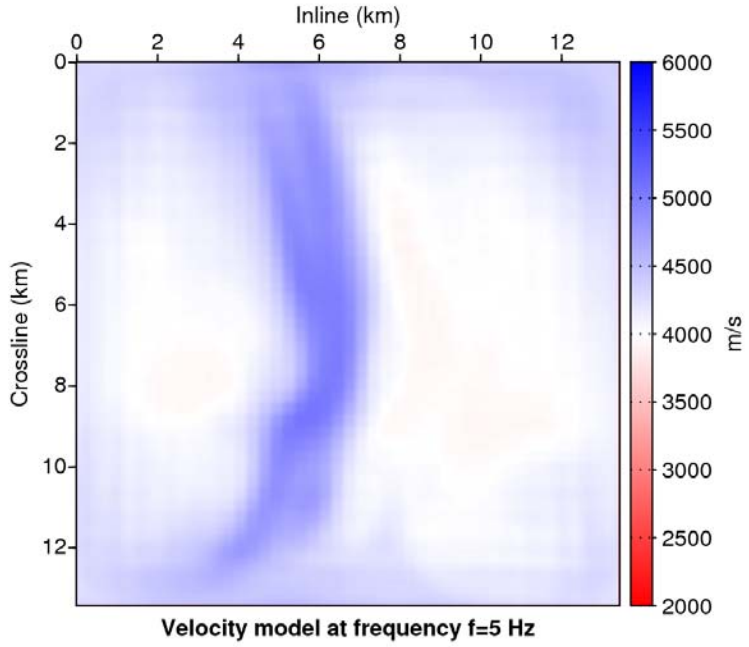

(a)

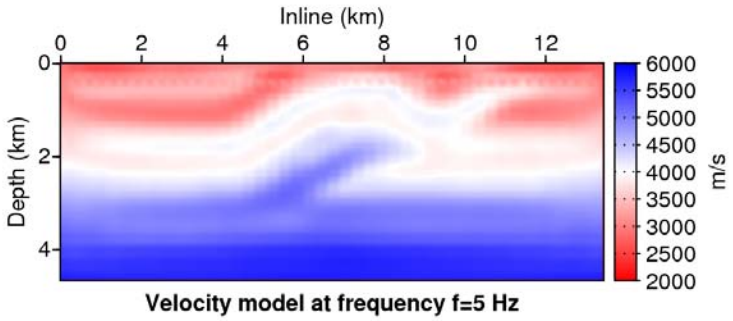

(b)

Figure 21: Imaging of the thrust system in the overthrust model: 5-Hz FWI velocity model. a) Horizontal slice at Z=2.3 km. b) Cross-section at X=6.75 km.

Ben Hadj Ali & al –

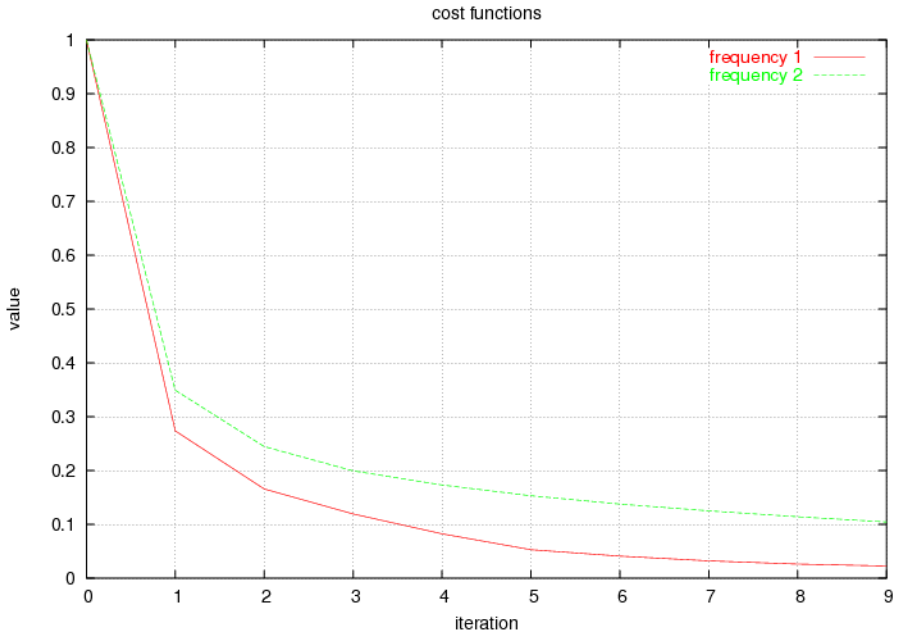

Figure 22: Imaging of the thrust system in the overthrust model: cost function versus iteration number for the 3.5-Hz and 5-Hz frequencies.

Ben Hadj Ali & al –

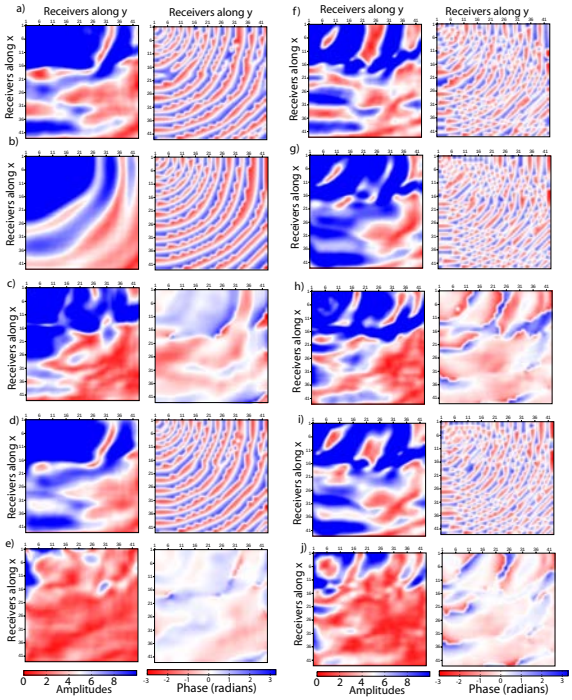

Figure 23: Imaging of the thrust system in the overthrust model: a) samplitude (left) and phase (right) of the 3.5-Hz monochromatic wavefield computed in the true velocity model at the receiver positions. The horizontal and vertical axis label the receiver number in the dip and cross directions respectively. The source is located in the upper-left corner of the receiver array. b) same than (a) but the wavefields were computed in the starting model of the 3.5-Hz inversion. c) Difference between maps shown in a) and b). d) Same than (a) but the wavefields were computed in the final model of the 3.5-Hz inversion. e) Difference between maps shown in (a) and (d). (f-j): same that for (a-e) but for the 5-Hz frequency.

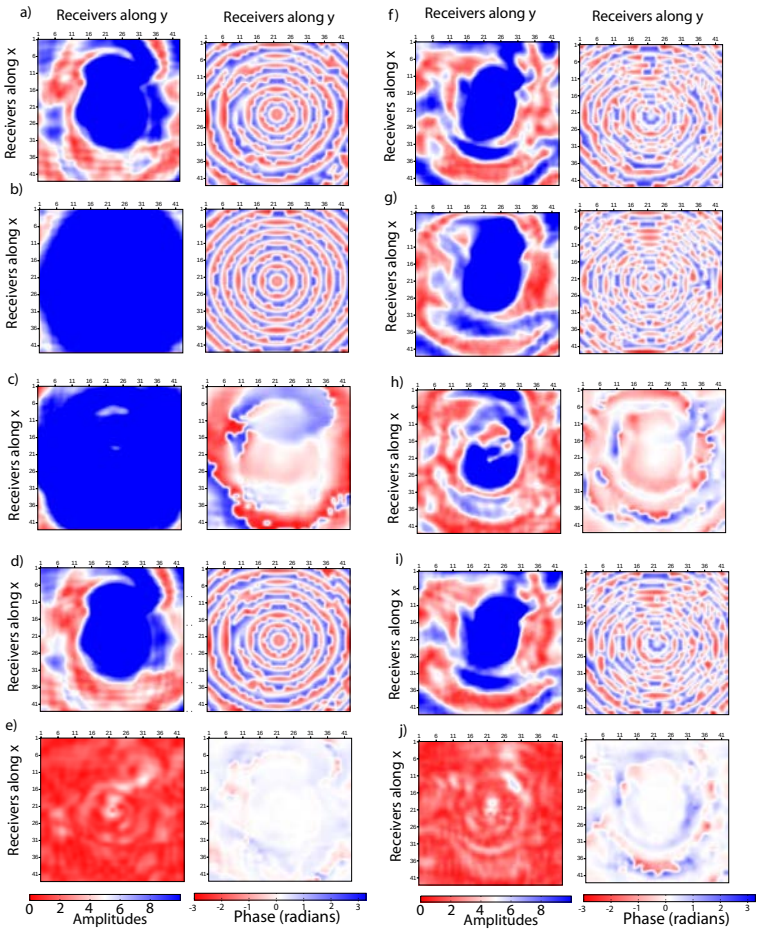

Figure 24: Imaging of the thrust system in the overthrust model: Same that for Figure 23 but for a source located in the middle of the receiver array.

Ben Hadj Ali & al –